Spatial variability of liquid water path in marine low cloud:

Part I. Probability distributions and mesoscale cellular scales.

ROBERT WOOD* and DENNIS. L. HARTMANN

University of Washington, Seattle, Washington

October 6, 2004

Corresponding author address: Dr. Robert Wood, Atmospheric Sciences, University of Washington, Seattle, WA; *e-mail: robwood@atmos.washington.edu.*

Abstract

Aspects of the liquid water path (LWP) spatial probability distribution function (pdf) and power spectra in marine low cloud over the subtropical NE and SE Pacific Ocean are examined using daytime retrievals for two months of data from the Moderate Resolution Imaging Spectroradiometer (MODIS) on the NASA Terra satellite. It is shown that the pdf can be described to a good degree of accuracy using a modified Gamma distribution in accordance with earlier work. The pdf is used to validate and constrain a simple Gaussian physical model of the mesoscale variability that links cloud LWP variability with the underlying boundary layer thermodynamical structure. Importantly, this model couples variability of the cloud LWP with the cloud fraction, and so may be used in large-scale numerical models to account for unresolved variability. Optical depth spatial variability is shown to be well modeled using an adiabatic assumption with constant droplet concentration. A simple formulation for albedo biases is presented that is implemented as a simple reduction in the cloud fraction. Power spectral analysis is used to determine the scale dependence of the LWP pdf. It is found that for the majority of power spectra, characteristic scales exist that are related to mesoscale cellular convection (MCC). However, despite the existence of characteristic scales in many cases, it is shown that in the ensemble, the liquid water path exhibits a surprisingly universal scaling with an exponent close to -5/3 over scales up to at least several hundred kilometers.

1. Introduction

Significant spatial variability in low (marine boundary layer, MBL) cloud structure exists on scales of metres to hundreds of kilometres (Cahalan and Snider 1989; Davis et al. 1996; Marshak et al. 1997; Wood and Taylor 2001). It is common for these clouds to self-organize into mesoscale cellular convection (MCC) (see reviews by Agee et al. 1973; Atkinson and Zhang 1996), with dominant horizontal scales much greater than the depth of the MBL. Such variability needs to be understood because of its importance in cloud-radiation interactions (Cahalan et al. 1994; Barker 1996a,b; Oreopoulos and Davies 1998a,b; Rossow et al. 2002), and in controlling the precipitatation rate (Rotstayn 2000; Pincus and Klein 2000; Larson et al. 2001; Wood et al. 2002; Stevens et al. 2004).

MCC can be of the open form (containing narrow regions of cloud around the cell edges and broad regions of clearing between) or closed form (broad regions of thick stratiform cloud in the cell centers often with relatively narrow regions of thinning or clearing at the edges). The MCC aspect ratios (cell center separation:BL depth) reported in field studies are typically 3-40 (Atkinson and Zhang 1996), significantly larger than those (usually 2-4) found in Bénard-Rayleigh (BR) convection. MCC is the predominant cloud structure for stratocumulus when the boundary layer is deeper than 1 km (Atkinson and Zhang 1996) and is found less often in very shallow stratus-topped boundary layers. A qualitative climatology of the prevalence of closed and open MCC over the global oceans was presented by (Agee et al. 1973), showing the tendency of closed cells to form over cold ocean currents and open cells to form over warm ocean currents. Attempts to model MCC have never been entirely successful at representing all its features (Rand 1995), and a set of criteria for predicting key features such as the aspect ratio, and whether the MCC will be open or closed, is still lacking.

Analysis of data from recent field campaigns (Davis et al. 1996; Marshak et al. 1997; Davis et al. 1999), shows that cloud liquid water content in MBL clouds exhibits multifractal scaling with inner scales of centimetres and outer horizontal scales that can be tens of km. Scaling exponents are similar to those for inertial subrange passive scalars. Although it has not been examined explicitly in most studies, this scaling appears to be one of the characteristic signatures of MCC. Many large-scale numerical model cloud schemes are based upon the prediction of the saturation excess pdf, the width of which is determined largely by variability on the mesoscale (e.g. Wood et al. 2002). In these models, the pdf width is often set equal to a fixed value in the lower troposphere. In reality, this pdf width has not yet been adequately constrained by observations nor has its links with MCC been explored. So far, the parameterization of saturation excess pdf width in the boundary layer (e.g. Bechtold et al. 1995; Cuijpers and Bechtold 1995) has implicitly assumed that the thermodynamic variance is dominated by large-eddy scales (~ 1 km). This, clearly, is not the case for most MBL clouds.

In this paper and its companion we examine aspects of the mesoscale spatial variability in low cloud over the ocean using satellite data. We use liquid water path as it is directly related to thermodynamic and structural characteristics. Initially, we look at probability density functions (pdfs). We then examine the scale dependence of the pdf properties using spectral analysis. In the second part of this study we present a climatology of the occurrence and characteristic of distinct types of mesoscale behavior in the NE and SE Pacific. NCEP/NCAR reanalysis data is used to understand the behavior of the cloud fields in relation to large scale forcings.

2. Details of MODIS data used

a. Instruments and physical parameter estimation

We use 1 km (at nadir) data from the Moderate Resolution Imaging Spectroradiometer (MODIS) on the NASA Terra polar-orbiting satellite (King et al. 1992). The MODIS cloud product uses visible/near-IR radiances (King et al. 1997) to derive optical thickness τ and near-cloud top effective radius $r_{e,top}$ resolution for daytime ($\sim$ 10:30 LST) scenes. Only those data that are within 45° of nadir (i.e. the central 1030 pixels of the scan) are used. Data from each granule are interpolated onto a 1$\times$1 km across- and along- track grid (1280 km across track, 2030 km along track).

Estimation of liquid water path LWP from the $r_{e,top}$ and τ requires a model of the cloud vertical structure. Often, the cloud is modelled as having constant liquid water content and $r_{e,top}$ in the vertical (e.g. Han et al. 1994) which gives $LWP = \frac{2}{3}\rho_w \tau r_{e,top}$, with ρ_w the density of liquid water. However, most observations of boundary layer clouds indicate that the liquid water content is an approximately linear function of height above cloud base, and that the cloud droplet concentration is approximately constant with height (e.g. Nicholls and Leighton 1986; Brenguier et al. 2000; Wood 2004). This model, used here, results in a relationship $LWP = \frac{5}{9}\rho_w \tau r_{e,top}$, giving LWP values a factor of 5/6=0.8$\dot{3}$ times those using the constant LWC, r_e model.

MBL depth z_i is estimated using the method presented in Wood and Bretherton (2004), a novel technique that uses cloud top and sea surface temperature, cloud liquid water path, and the simple model of Park et al. (2004). Estimates of the accuracy of this techinique suggest that the uncertainty in each z_i estimate is approximately 200-300 m (Wood and Bretherton 2004).

b. Analysis methods

Our basic unit of analysis is a "scene", a 256×256 (km)^2 portion of the MODIS swath. Power spectra from regions larger than this tend to show a spectral gap at scales of 20-200 km. This spectral gap occurs at considerably larger scales than the classic spectral gap (see e.g. Van der Hoven 1957; Stull 1988), and is highly variable in wavenumber. Our choice of scene size therefore represents the desire to capture most of the mesoscale cellular variability while having a small enough area so that sufficient numbers of scenes are free of high cloud. The choice also reflects our desire to be able to examine how LWP statistics vary geographically. We also note that the chosen size is representative of the scale of a current GCM gridbox. Scenes containing only warm cloud are selected using the MODIS thermal IR cloud top temperature (Ma et al. 2000). Only wholly oceanic scenes are analyzed. Some scenes are rejected because of clear instrumental or calibration errors resulting in unphysically large τ. The occurrence of such scenes is uncorrelated with cloud characteristics and so should not bias the results.

Two regions of the East Pacific dominated by low cloud are chosen for this study (see Table 1). All available data from September/October 2000 are used. Figure 1 shows the regions, together with contours that give the fraction of MODIS scenes accepted for analysis. The ISCCP Rossow and Schiffer (1991) 16 year climatological mid+high cloud amount for September/October (assuming random overlap) is also shown. Over much of the two regions, particularly in the SE Pacific, the mid+high cloud amount is less than 10-15% and the fraction of scenes analysed exceeds 50%, demonstrating the dominance of low cloud, and the lack of high clouds to the east of the subtropical gyres. This fraction decreases both equatorward, due to the presence of clouds associated with deep convection, and towards the midlatitudes, where deep frontal clouds are prevalent.

The curious peak in ISCCP mid+high cloud off the coast of southern Peru/northern Chile probably reflects a misdiagnosis of low clouds as midlevel clouds caused by the extremely strong inversions representative of this region.

This study is concerned with the spatial variability of LWP and its dependence upon spatial scale. We use (a) one-point statistics (pdfs), and (b) power spectral analysis to examine variance as a function of spatial scale. Scenes are overlapped by 128 km in each direction to approximately restore the degrees of freedom lost through data windowing (Welch window).

3. Forms and models for LWP probability density function

Finding a suitable analytical pdf to represent LWP will provide a framework for characterisation of cloud variability and will be useful in the parameterisation of cloud inhomogeneity. Oreopoulos and Davies (1998b) examine distributions of τ from AVHRR satellite data, fitting them using gamma, beta and lognormal distributions. They conclude that the gamma distribution gives the poorest fit for purposes of correcting albedo biases. However, they do suggest that in many cases the poor fit is a result of a small number of very large τ values which distort the variance, and are the likely result of using mixtures of different cloud types. The gamma distribution has been used to characterise τ distributions in boundary layer clouds (Barker 1996b; Oreopoulos and Davies 1998a) and performed as well as the lognormal distribution. The choice of a pdf form depends upon its purpose. For albedo bias corrections accuracy of the low moments (between 0th and 1st order) is paramount because albedo-τ curves are concave, whereas higher order moments are important for precipitation (Wood et al. 2002). In this study we concentrate on four distribution forms, described below, to model the LWP pdf and its moments (see Table 3).

a. Gamma distribution

The form of the two-parameter gamma (Γ) distribution is

$$P_{\Gamma}(x) = \frac{1}{\Gamma(\gamma_x)} \left(\frac{\gamma_x}{\overline{x}}\right)^{\gamma_x} x^{\gamma_x - 1} \exp\left(-\frac{\gamma_x x}{\overline{x}}\right) \tag{1}$$

where $\overline{x}$ and σ_x are the mean and standard deviation of x, and $\gamma_x = (\overline{x}/\sigma_x)^2$. There are two options for obtaining the parameters $\overline{x}$ and γ_x for the Γ distribution from the observed LWP field: (a) the method of moments (MOM); (b) maximum likelihood estimaton (MLE). The MOM uses the observed mean $\overline{x_{obs}}$ and standard deviation $\sigma_{x,obs}$ (i.e. moments of order 1 and 2) of x to calculate γ_x directly. The MLE method uses $\overline{x_{obs}}$ and $\overline{\ln(x_{obs})}$, also calculable from the pdf of x, to estimate γ_x (see Oreopoulos and Davies 1998b). The MLE is less sensitive to the high x tail of the distribution than is the MOM. We examine the consequences of this in Section **3.4.**

b. Lognormal distribution

The two-parameter lognormal (LN) distribution is given by

$$P_{LN}(x) = \frac{1}{sx\sqrt{2\pi}} \exp\left[-\frac{(\ln x - \mu)^2}{2s^2}\right] \tag{2}$$

where $\mu = \overline{\ln x}$, and $s = \sigma_{\ln x}$. For the LN distribution, μ and s are analytically related to $\overline{x}$ and σ_x.

c. Gaussian distributions

The last two pdf types examined here result from physical models that link LWP variability with variability in other physical parameters. Such linkages may prove useful in the task of physical

parameterization. The Gaussian cloud thickness model (Gaussian-h model) is presented in Considine et al. (1997), expanded upon in Jeffery and Austin (2003), and is supported by observations in unbroken stratocumulus (Wood and Taylor 2001). Its applicability to broken clouds is unknown, although there is evidence to indicate its utility in modeling broken MBL cloud (Park et al. 2004). The Gaussian-h model nondimensional LWP variability, expressed using the parameter $\gamma_{LWP} = (\overline{LWP}/\sigma_{LWP})^2$, is related to the area cloud fraction (CF) using a single scale-independent function.

The Gaussian-h model results in a LWP pdf, for the cloudy fraction CF of the region, that is a function of two inputs: the mean $\overline{h}$ and standard deviation σ_h of the distance h between the cloud top (inversion) and base (LCL):

$$P_{\text{Gaussian}-h} = \frac{1}{CF\ \Gamma h\sqrt{2\pi}} \exp\left\{-\frac{(h-\overline{h})^2}{2\sigma_h^2}\right\} \qquad (h > 0) \tag{3}$$

where

$$CF = \frac{1}{2}\left\{1 + \text{erf}(\overline{h}/\sqrt{2}\sigma_h)\right\} \tag{4}$$

and Γ is the vertical gradient of liquid water content, which we assume to be equal to the adiabatic value Γ_{ad} throughout this study. See Jeffery and Austin (2003) for addition exploration of this model. Note that values of $h < 0$ indicate those regions where the inversion is lower than the LCL and are therefore cloud-free. Only a weak dependence upon atmospheric pressure and temperature exists (through Γ_{ad}) within subtropical regions (Considine et al. 1997).

A Gaussian distribution of saturation excess (Gaussian-s model) also leads to a LWP pdf through the assumption that $\overline{q_t} - q_{sat}(\overline{T_l}, p)$ increases linearly with height in the MBL, where q_t is the total water content and q_{sat} is the saturation specific humidity. The liquid temperature T_l is defined as $T_l = T - L_v q_l/c_p$, where q_l is the liquid water content, and L_v and c_p are the specific

heat of condensation of water and the specific heat capacity of air respectively. In a boundary layer that is vertically well-mixed, $\theta_l\,(=\,T_l\,\theta/T)$ and q_t are conserved, leading to a near-linear increase in saturation excess with height for clouds of small vertical extent. Maximum overlap of clouds is assumed and the pdf width is assumed constant in any given scene at all levels in cloud. The Gaussian-s model is used in this study in conjunction with MODIS observed LWP pdfs to derive estimates of the saturation excess standard deviation σ_s, where saturation excess is defined (Sommeria and Deardorff 1977) as $s = \{q_t - q_{sat}(T_l, p)\} \,/\, \left\{1 + \frac{L_v}{c_p}\left(\frac{\partial q_{sat}}{\partial T}\right)_{T_l}\right\}$.

Conceptually one can think of the LWP pdf as a reflection of the underlying pdf of s. The use of a pdf of s to represent partial cloudiness has its roots in the work of Sommeria and Deardorff (1977) and Mellor (1977), and is the basis for a number of large-scale parameterizations (e.g. Smith 1990; Lewellen and Yoh 1993). For zero cloud top fluctuations, the Gaussian-h model and the Gaussian-s models are equivalent. Even without this assumption, the forms of the LWP pdfs are the same for the two models; zero cloud top fluctuations allows equivalence between h and s, so that a 1:1 mapping exists between $[\overline{LWP}, CF]$ and $[\overline{s_i}, \sigma_s]$ (or equivalently $[\overline{h}, \sigma_h]$), where s_i is the saturation excess at the inversion base. The variables h and s are linearly related because boundary layer clouds are thin enough that the liquid water content (or, equivalently, s) increases linearly with height. We can write relationships between the h and s means and variances:

$$\overline{s_i} \;=\; \Gamma\overline{h}; \tag{5}$$

$$\sigma_s \;=\; \Gamma\sigma_h. \tag{6}$$

For the temperature and pressure range of the clouds observed in the NE and SE Pacific, the 5th, 50th and 95th percentiles of $\Gamma \,=\, \Gamma_{ad}$ are 1.66, 1.92 and 2.13 g kg^{-1} km^{-1} respectively. The assumption of adiabaticity is not a necessary condition for the model, but is used here to provide

clarity, and is supported by observations in MBL clouds (Albrecht et al. 1990; Bretherton et al. 2004).

4. Observations of liquid water path pdfs

a. Example scenes

We use MODIS data to estimate the suitability of the pdfs described above to describe LWP spatial variability for the cloudy fraction of the scene. To demonstrate the range of observed distributions of LWP we use four test scenes containing boundary layer cloud types and structures representative of the range found in MBL clouds (Fig. 2). Scene (a) contains relatively homogeneous stratus which is common in near coastal waters in the NE Pacific. Scene (b) contains relatively unbroken stratocumulus cloud with small mesoscale convective cells typical of the extensive stratocumulus sheets over the oceans to the west of continents. Scene (c) contains large stratocumulus cells with breaks typical of the transition regions in the trade wind boundary layers. Scene (d) contains open-celled convective clouds, particularly common in the SE Pacific (see Part II). The MODIS cloud mask (Ackerman et al. 2002) is used to determine the fraction of cloudy pixels, i.e. CF. Dates and locations, together with a number of parameters obtained for each of these scenes are given in Table 2.

The LWP pdfs for the four test scenes are shown in Fig. 3(a,b). Although the LN distribution appears to be a better match to observations at low values of LWP for scenes (c) and (d), the LN is too broad at high LWP. In all cases, observed tails are narrower than those from the LN model, and match better with those from the Γ distribution. Liquid water path observations become very unreliable for $LWP < 10$ g m^{-2} and the pdfs often become more noisy and unreliable at these

values.

b. Moments of the LWP distribution

Relationships between the second order moments and higher moments (skewness S and kurtosis K) are shown in Fig. 4. It is important to emphasize that the LWP statistics are over cloudy pixels only (i.e. zeros are excluded). Each model pdf form has a different but unique relationship between these moments. The LN pdf overestimates skewness and kurtosis for any given value of γ_{LWP}. This is undesirable from the point of view of being able to represent higher order moments. The other pdf forms considered provide quite realistic relations between the different moments of the LWP distribution.

Figures 5 and 6 show the cumulative contribution to the moments of order 0.5 and 3 respectively as a function of LWP. For moment order 0.5, all models perform well. These results further confirm the LN overestimation of higher order moments, especially in the more heterogeneous cases (c and d). Both the Γ and Gaussian pdfs perform well. The overestimation of higher order moments by the LN distribution is a general result, and worsens as relative LWP variability increases. We conclude that the Γ distribution is a more appropriate descriptior of the LWP pdf than the LN, and that the Gaussian model also produces realistic pdfs.

c. Relationship between LWP moments and cloud fraction

Figure 7 shows the relationship between CF and $\gamma_{LWP} = (\overline{LWP}/\sigma_{LWP})^2$ for all the SE Pacific scenes and the unique relationship corresponding to the Gaussian model. The NE Pacific data (not shown) are very similar. Although both observations and models exhibit a similar behavior,

with γ_{LWP} increasing as CF approaches unity, in almost all cases the observed LWP fields are less variable (higher γ_{LWP}) than the Gaussian model at a particular CF. Indeed, the Gaussian curve appears to form the lower limit of the observations. This is surprising given that Wood et al. (2002) find that aircraft-derived CF is well modeled using the Gaussian distribution of s. Possible explanations are (a) that, in general, any one scene does not contain a single statistical regime and that this degree of statistical nonstationarity results in changes to the $CF - \gamma_{LWP}$ relationship; (b) that the observed fields tend to have larger values of γ_{LWP} because cloudy pixels with low LWP values are categorized as clear sky. It is clear that effect (b) would always result in observed CF and γ_{LWP} values that are too low and too high respectively, but it is not clear what the magnitude of this effect is.

To assess (a) above, we obtain a quantitative measure of the statistical stationarity in the scenes using (i) the degree to which a plane surface fit removed from the LWP field reduces its variance, and (ii) the reduction in variance that is obtained when applying the Welch window. For a stationary variable (defined here as one for which the mean and variance are invariant in translations), the plane surface fit will remove only a small fraction of the variance, because the mean does not vary in space. Because the scene variance is invariant to translations, the Welch window $W(x, y)$ will reduce the scene variance by a factor equal to the inverse of the normalized integral of the square of $W(x, y)$ over the scene, i.e. $L^2/(\int_0^L \int_0^L W(x, y)^2 dxdy) = 225/64 = 3.52$, where L is the side length.

We choose those scenes for which the surface fit removal reduces the variance by less than 10% (37% of scenes) *and* the Welch window reduces the variance by a factor of 3.02-4.02 (35% of scenes), giving a total of 1377 "stationary" scenes for the NE Pacific data. We also find the least "stationary" scenes (1602 scenes) by selecting those scenes for which the surface fit removal re-

duces the variance by more than 15% (31% of scenes) *and* the Welch window reduces the variance by less than a factor 2.77 or more than a factor 4.27 (51% of scenes). We examine the $CF - \gamma_{LWP}$ relationship for both sets of scenes by binning as a function of CF (Fig. 8). The stationary scenes tend to have smaller γ_{LWP} than the least stationary scenes, with the greatest differences for $0.6 < CF < 0.9$, but the most stationary scenes still have LWP fields that remain considerably more homogeneous than the corresponding Gaussian models. This indicates that the mixing of statistically distinct regimes (as in the least stationary scenes), is not the dominant factor for the disparity between the Gaussian model and the data.

The thresholding issue (b) above is addressed by deriving CF and γ_{LWP} only for LWP values greater than some threshold value LWP_{thresh}. The same thresholding is applied to the Gaussian model pdfs. A reasonable value of LWP_{thresh} is 5 g m^{-2}, as this corresponds to $\tau \sim 1$ for MBL clouds, and this is close to the limit of detectability in the MODIS-observed τ. For the thresholded data, CF values are smaller (median reduction 0.013) and γ_{LWP} values generally higher (median increase 0.047). This does not represent a particularly large change. However, when we apply the same thresholding to the Gaussian pdfs, we find marked differences that bring the observations and model results into much closer agreement (Fig. 9). We conclude that much of the disagreement between measured and modeled $CF - \gamma_{LWP}$ in Fig. 7 is due to differences in the observed and modeled distributions for $LWP < 5$ g m^{-2}. While there may be some real differences at these low values of LWP, the measurement uncertainties preclude further investigation. The use of lidar may be useful in addressing these low LWP issues. We conclude that the Gaussian model is a reasonable descriptor of the relationships between LWP variability and cloud fraction for low marine, at least for $LWP > 5$ g m^{-2}. Throughout the remainder of this study, all one-point statistics presented are derived using a LWP threshold of 5 g m^{-2} to define the presence of cloud.

Figure 10 shows the 1:1 mapping between [$\overline{LWP}$, CF] and [$\overline{h}$, σ_h], ([$\overline{s_i}$, σ_{s_i}]), for all SE Pacific MODIS scenes. For accordance between h and s it is assumed that the cloud layer is adiabatic with a constant Γ_{ad}=2 g kg^{-1} km^{-1}. Using this mapping, two interesting and important points emerge. First, the MODIS data are clustered around $\overline{LWP}$ isolines, so that only rarely do scenes have mean LWP larger than 150 g m^{-2} or less than 25 g m^{-2}. This represents a range of adiabatic cloud thickness of only 200 m, which is surprisingly small given the range of MBL depth (500-2500 m). Also surprising is that these limits seem to be relatively independent of CF suggesting that there may be universal physical upper and lower limits upon cloud liquid water path in MBL clouds. We hypothesize that the upper limit is imposed by a negative drizzle feedback. Increased LWP produces more drizzle which stabilizes the MBL and suppresses moisture transport from the surface, thus reducing LWP. The lower limit may be associated with longwave radiative feedback that results in instability in very thin cloud layers, which either rapidly thicken or dissipate (Paluch and Lenschow 1991). Indeed, radiative transfer calculations suggest that the longwave cooling efficiency starts to weaken in clouds with LWP less than 25-50 g m^{-2}. Second, σ_h (or σ_s) is inversely correlated with $\overline{h}$ (or $\overline{s_i}$) as the clouds transition from overcast stratocumulus to broken trade-wind cumulus. This increasing mesoscale variability in the Sc-Cu transition is strongly related to the properties of the MCC and boundary layer depth (see Part II of this study), with the source of variability in h (or s) related to the increasing decoupling of the cloud layer from the surface mixed layer.

d. Relationship between LWP and τ variability

Optical thickness spatial variability is strongly related to that in LWP, but the exact relationship depends upon the ratio of the variability in the droplet concentration (or cloud-top effective radius $r_{e,top}$) to that in the LWP, and upon the degree of correlation between these two fields (Szczodrak et al. 2001). Considering the case where the cloud droplet concentration N_d has no height variability, for an adiabatic cloud, local τ is proportional to $LWP^{5/6}$ (Szczodrak et al. 2001). With this simple linear transform, assuming no horizontal variability in N_d, for the Γ distribution of LWP:

$$\gamma_\tau = \left(\frac{6}{5}\right)^2 \gamma_{LWP} = 1.44\gamma_{LWP} \tag{7}$$

where $\gamma_\tau = (\overline{\tau}/\sigma_\tau)^2$. For the special case where the liquid water path and $r_{e,top}$ are completely uncorrelated, one finds

$$\gamma_\tau = \left(\gamma_{LWP}^{-1} + \gamma_{re}^{-1}\right)^{-1} \tag{8}$$

where $\gamma_{r_e} = (\overline{r_e}/\sigma_{r_e})^2$. Figure 11 shows that in general, the observed τ fields are less variable than the LWP fields ($\gamma_\tau > \gamma_{LWP}$), because positive correlations usually exist between LWP and $r_{e,top}$. This behavior is expected for an adiabatic cloud with a weakly variable droplet concentration (Eqn. 7). The inset shows that $r_{e,top}$ fields are much less variable than the LWP fields (5th and 95th percentiles of $\gamma_{r_e}/\gamma_{LWP}$ are 2.5 and 12.4 respectively). The shaded regions in Fig. 11 show the range of values of γ_{LWP} and γ_τ for uncorrelated LWP and $r_{e,top}$ (darker shading) and for uncorrelated LWP and N_d (lighter shading), indicating that the observed γ_τ-γ_{LWP} relationship is most consistent with an model in which LWP and N_d are uncorrelated and the mesoscale variability of droplet concentration is quite weak ($\gamma_{N_d}/\gamma_{LWP}$ is approximately lognormally distributed with 5th and 95th percentiles equal to 1.7 and 32.5). This result generalizes the findings in Szczodrak et al. (2001), who examined 31 stratocumulus scenes from the Advanced Very High Resolution

Radiometer (AVHRR) in the NE Pacific.

e. Albedo biases

The mean albedo of an unbroken but inhomogeneous cloud field depends upon both the mean and the spatial variability of τ. (Cahalan et al. 1994; Oreopoulos and Davies 1998a). Mean albedo decreases for increased variability given fixed $\overline{\tau}$ because local albedo A is a concave downward function of local τ for all zenith angles θ_0. The mean albedo $\overline{A}$ of a partially cloudy region is therefore dependent upon CF, the clear sky albedo A_{CLR}, and the pdf of τ in the cloudy fraction of the region. There have been a number of attempts to quantify the magnitude of the albedo bias that results when spatial variability is ignored. Cahalan et al. (1994) overestimated the typical errors that are likely for a GCM gridbox because an overly broad pdf of liquid water path taken over several days of observations was used. Here, our 256$\times$256 km regions are similar in size to a GCM grid-box, and we assess the magnitude of the albedo bias by asking the question *what reduction in cloud fraction is required to obtain the correct mean albedo while treating the cloudy portion of the domain as a homogeneous cloud having the same $\overline{\tau}$ (as the observed heterogeneous cloud)?*.

Some simple manipulation leads to a reduction ΔCF in cloud fraction CF, where

$$\Delta CF = CF \frac{A(\overline{\tau}, \theta_0) - \overline{A(\tau, \theta_0)}}{A(\overline{\tau}, \theta_0) - A_{CLR}}. \tag{9}$$

Here, $A(\overline{\tau}, \theta_0)$ is the albedo of the cloudy fraction calculated using the mean τ (i.e. the homogeneous cloud albedo), and $\overline{A(\tau, \theta_0)}$ is the true albedo of the (heterogeneous) cloudy fraction. Considering radiative transfer through the MBL only using Fu and Liou (1992) we find that

A_{CLR}=0.04-0.06 in subtropical and lower midlatitude MBLs for zenith angles $< 60°$. We assume a constant value $A_{CLR} = 0.05$ but note that our results are quite insensitive to the precise choice.

An advantage of the ΔCF measure of albedo bias is that it is almost insensitive to θ_0 for $\theta_0 < 60°$. Figure 12 shows ΔCF as a function of CF and θ_0. Because cloud homogeneity and cloud fraction are tightly coupled, there is a tight relationship between ΔCF and CF. For $CF < 0.8$, ΔCF increases approximately linearly with CF because LWP variability (γ_{LWP}) is not a strong function of CF (Section **3.4.**). At larger CF, ΔCF reduces as internal homogeneity in LWP increases sharply with CF. It is possible to use this relationship as the basis for a simple, yet quite effective, parameterization of the albedo of inhomogeneous MBL cloud fields. The reduced cloud fraction $CF - \Delta CF$ could be used with little computational cost in a radiative transfer scheme to account for unresolved spatial variability. The correction $\Delta CF < 0.2$ in almost all cases, suggesting that cloud spatial variability is a significant modulator of the mean albedo. Although temporal variability in CF (see Fig. 8 in Part II of this paper), largely controls variability in shortwave cloud forcing on timescales of days to months, the contribution of mesoscale variability is important (see also Rossow et al. 2002).

5. Scale dependence of the pdf

Little attention has been paid to the scale dependence of cloud and boundary layer process parameterizations. Increasingly, cloud schemes in GCMs use pdf formulations to describe subgrid variability in thermodynamic and cloud properties. However, until the paper by Cusack et al. (1999), little attempt had been made to treat the pdf widths either as variables or as scale-dependent parameters in large-scale numerical models. Because of the current lack of observational constraints, pdf widths are used essentially as tunable parameters in GCMs to balance top-of-atmosphere radiation

budgets. This is an undesirable situation and warrants attention.

Spectral and structure function analysis reveals that pdf widths of a range of cloud parameters increase as the scale increases (e.g. LWP, Cahalan and Snider (1989); liquid water content, Davis et al. (1996); cloud base height, Wood and Taylor (2001); drizzle precipitation rate, Wood (2004)). Cusack et al. (1999) applies a 5/3 scaling exponent to parameterize subgridscale variability of the small scales (< 300 km) based upon the resolved scales (variance of 3×3 gridboxes). There is some evidence of a universal scaling of cloud properties over this range (Lovejoy 1982), but the compositing of a large number of different cloud scenes and regimes to form a single scaling function may miss features that interfere with the simple power law scaling. Here we use MODIS data to examine scaling issues.

a. Power spectra and characteristic lengthscales

For each scene we derive the 2D power spectrum as a function of total wavenumber k, where $k^2 = k_x^2 + k_y^2$ and k_x, k_y are the wavenumbers along the axes of the square scene. The image is first detrended by removing the best-fit plane and then windowed using a 2D Welch window. Power spectra for the four test scenes are shown in Fig. 13. We find that spectra for both open and closed MCC usually exhibit a peak at some lengthscale (this lengthscale we call λ_1). Power law scaling is generally found at large k. The scale at which the spectrum diverges from the power law we label as λ_2. Closed MCC spectra diverge from the power law at a scale close to the peak scale (i.e. $\lambda_1 \approx \lambda_2$, as in Fig. 13(b) and (c)), but for open MCC the divergence from power law behavior occurs at a scale somewhat smaller than the cell-scale (i.e. $\lambda_1 > \lambda_2$, as in Fig. 13(b) and (c)). Visual inspection of many scenes leads to the conclusion that λ_1 and λ_2 can be interpreted

as the approximate cell diameter and typical cloud size respectively. For closed cells these are approximately the same because the gaps between clouds are quite small. Open MCC tends to consist of small clouds that form around the perimeter of a larger cellular structure.

We devised methods to determine automatically the lengthscales λ_1 and λ_2 from the power spectral data. In some cases the power law behavior is either not present or limited to scales similar to the Nyquist frequency (0.5 km^{-1}) and cannot be determined using the MODIS data. In these cases λ_2 is undefined. Similarly, some of the scenes do not contain a peak in the power spectrum other than that introduced artificially by data windowing. In such cases λ_1 is undefined.

Composite LWP power spectra for different ranges of the cell size λ_1 are are shown in Fig. 14. An approximate power law scaling of the high wavenumber tail with an exponent in the range 1.4-2.0 is demonstrated in accordance with previous observations. It is also clear that an increase in cell size is, on average, associated with an increase in LWP variance. We scrutinize further the links between LWP variance and the cell size in Part II of this study.

b. The ensemble picture

We have seen that a characteristic cell lengthscale λ_1 is often found in the LWP power spectrum, which might lead one to the conclusion that this demonstrates a violation in the $\beta-$ and $\gamma-$mesoscale of the universal scaling relations found by Lovejoy (1982). While this does indeed show that local departures from any universal scaling law do exist, it is not clear from the analysis in Section **5.**a. whether or not a universal scaling law exists in an ensemble sense. To investigate this we generate realizations, using an inverse FFT fractal model (Peitgen and Saupe 1988), of liquid water path superscenes (2×2 scenes) that exhbit power law scaling (with exponent β) from

1-512 km. We then split the 512×512 km region into four 256×256 km scenes. For each of the four scenes we obtain the mean $\overline{x_{i,j}}(i = 0, 1; j = 0, 1)$ and standard deviation $\sigma_{i,j}$ of the LWP for just the cloudy portion. We find the ratio α of the mean of the four standard deviations to the standard deviation of the four means $\alpha = \overline{\sigma_{i,j}}/\sigma_{\overline{x_{i,j}}}$. The process is repeated to build up a distribution of α values from many simulations with different scaling exponents β. The magnitude of α determines the ratio of the power that is in scales smaller than the scene size to the power at scales larger than the scene size, and so can be used to validate the parameterization of Cusack et al. (1999) because the above approach can also be carried out with groups of 2×2 adjacent scenes.

Figure 15 shows distributions of α values from the MODIS datasets. All scenes with $CF > 0.1$ are included. Also shown is the model distribution for a scaling exponent of $\beta = -1.4$ which matches fairly well with the observations. The inset shows that the MODIS data are consistent with an ensemble scaling exponent close to -1.4. This result is somewhat surprising in the light of the findings that most individual scenes have a characteristic scale and therefore a scale break. In spite of this, it appears that nature conspires to maintain a universal scaling *in the ensemble* throughout much of the mesoscale, even though individual realizations have distinct scale breaks. It may therefore be a reasonable approach to base parameterizations of subgridscale variability upon model-resolved variability at larger scales, although there is a lack of a clear physical mechanism to link the mesoscale cellular convection to variability on scales > 100 km. A recent sensitivity study (Williams et al. 2003) demonstrates that the introduction of the Cusack et al. (1999) subgrid parameterization has a marked impact upon cloud feedbacks in the Hadley Centre GCM. It seems to be imperative therefore that the pdf width of thermodynamic variables is treated as an important variable in GCMs.

6. Mesoscale cellular convection types

a. Scene type classification

The LWP pdf and the power spectrum are used to classify scenes into four categories that encompass the range of mesoscale (1-100 km) structures in low clouds: (i) homogeneous cloud with no MCC; (ii) closed MCC; (iii) open MCC; (iv) heterogeneous cloud without clear MCC. We use a neural network technique because of its powerful pattern recognition abilities. An introduction to neural networks in remote sensing can be found in Atkinson and Tatnall (1997), with more specific application to cloud classification in Clark and Boyce (1999) and Schroder et al. (2002). We use a simple 3-layer back propagation network (Castleman 1996) with the feature vector containing 72 elements, the first 32 being a resampling of the LWP power spectrum, and the latter 40 being a resampling of the LWP pdf. Approximately 1000 scenes were classified by eye as belonging to one of the categories (i)-(iv) above, and this ensemble was used to provide equally sized training and verification datasets. Training is carried out until the misclassification in the verification dataset ceases to decrease. We obtained a 85-90% classification accuracy for the trained network. Visual inspection shows that misclassified scenes tend to have features common to two categories, i.e. are those that are more difficult to classify for the human observer. The neural network weights derived from the training process are then applied to all MODIS data from the NE and SE Pacific to provide a scene-by-scene classification.

b. Scene type properties

Probability density functions of cloud fraction CF for each of the four categories are shown in Figure 16. Homogeneous scenes exhibit the broadest pdf of CF, which is bimodal with peaks at high and low CF. Closed MCC has high cloud fraction, with over 50% of scenes having $CF > 0.85$. Open MCC exhibits a peak at $CF = 0.4$, but scenes with high CF are also found. Heterogeneous clouds lacking clear MCC tend to have low CF, but again there is a tail extending to high CF.

We examine the effect of MBL depth z_i upon scene type by examining the fraction of scenes classified in each category as a function of z_i (Fig. 17). Homogeneous scenes are predominantly found to occur in shallow MBLs (50% of all scenes with $z_i < 500$ m are of this type). For $z_i > 1000$ m homogeneous scenes contribute only 10% to the total. The fraction of closed MCC peaks at 40% of all scenes for $z_i \approx 1000$ m before falling to around 15% for $z_i > 1500$ m. Open MCC peaks for z_i in the range 1000-1500 m but its prevalence does not markedly decline in the deeper MBLs. Heterogeneous scenes without MCC are not common in shallow MBLs, but are approximately as common as open+closed MCC combined for $z_i > 1500$ m. In Part II of this study we examine the geographical distribution of the different scene types and describe a conceptual model of the evolution of the mesoscale structures and cloud variability along subtropical trajectories.

7. Discussion and conclusions

A number of analytical tools have been applied to kilometer resolution visible satellite data to determine characteristics of LWP spatial variability in MBL clouds. Two regions, both dominated by marine low cloud, form the focus of our study. One-point (pdfs) and two-point (power spectra)

measures have been used to characterize the spatial variability. We have demonstrated that the gamma pdf proposed by Barker (1996a) describes the LWP pdf well. In addition, the LWP pdf arising from a Gaussian model of saturation excess is also suitable, and has the advantage of linking thermodynamic variability with radiative properties.

Through examination of the liquid water path mesoscale variability of subtropical MBL clouds, we have demonstrated that a tight link exists between the triad of parameters $\overline{LWP}$, γ_{LWP} and the cloud fraction CF. The cloud fraction is closely related to spatial variability of the LWP of the cloudy region. The findings provide solid observational support for the general philosophical approach to parameterizing the cloud structural properties using a saturation excess probability density function (pdf), as suggested initially by Sommeria and Deardorff (1977) and Mellor (1977). The use of these statistical schemes in large-scale numerical models (e.g. Smith 1990; Tompkins 2002) has met with a substantial amount of criticism, and some of this stems from the unconstrained nature of the underlying saturation excess pdf, particularly the pdf's width that has been used in many large-scale numerical models as a tunable parameter to balance top-of-atmosphere radiation budgets. Part II of this study describes a new set of constraints upon the mesoscale variability and pdf width, through links with the boundary layer depth.

Using Fourier analysis we find that the LWP power spectra often exhibit a peak in the mesoscale (5-100 km) range, and that this is associated with mesoscale convective cells clearly observed in the satellite images. However, taking the ensemble over all the images, we find that there appears to be robust universal scaling throughout the mesoscale range. Thus locally the universal scaling can, and often is, violated, but appears to be maintained over long time and space scales.

In a second study we construct a simple climatology of spatial variability properties over the NE and SE Pacific, and examine its dependence upon large scale meteorological variables.

References

Ackerman, S. A., K. Strabala, P. Menzel, R. Frey, C. Moeller, L. Gumley, B. Baum, S. Wetzel Seeman, and H. Zhang: 2002, Discriminating clear-sky from cloud with modis. MODIS Algorithm Theoretical Basis Document MOD35 ATBD-MOD-06, NASA.

Agee, E. M., T. S. Chen, and K. E. Dowell: 1973, A review of mesoscale cellular convection. *Bull. Amer. Meteorol. Soc.*, **54**, 1004–1012.

Albrecht, B. A., C. W. Fairall, D. W. Thomson, A. B. White, J. B. Snider, and W. H. Schubert: 1990, Surface-based remote-sensing of the observed and the adiabatic liquid water content of stratocumulus clouds. *Geophys. Res. Lett.*, **17**, 89–92.

Atkinson, B. W. and J. W. Zhang: 1996, Mesoscale shallow convection in the atmosphere. *Rev. Geophys.*, **34**, 403–431.

Atkinson, P. M. and A. R. L. Tatnall: 1997, Neural networks in remote sensing. *Int. J. Remote Sensing*, **18**, 699–709.

Barker, H. W.: 1996a, A parameterization for computing grid-averaged solar fluxes for inhomogeneous marine boundary layer clouds. Part 1: Methodology and homogeneous biases. *J. Atmos. Sci.*, **53**, 2289–2303.

— 1996b, A parameterization for computing grid-averaged solar fluxes for inhomogeneous marine boundary layer clouds. Part 2: Validation using satellite data. *J. Atmos. Sci.*, **53**, 2304–2316.

Bechtold, P., J. W. M. Cuipers, P. Mascart, and P. Trouilhet: 1995, Modeling of trade wind cu-

muli with a low-order turbulence model: toward a unified description of cu and sc clouds in meteorological models. *J. Atmos. Sci.*, **52**, 455–463.

Brenguier, J. L., P. Y. Chuang, Y. Fouquart, D. W. Johnson, F. Parol, H. Pawlowska, J. Pelon, L. Schuller, F. Schroder, and J. Snider: 2000, An overview of the ACE-2 cloudycolumn closure experiment. *Tellus*, **52B**, 815–827.

Bretherton, C. S., T. Uttal, C. W. Fairall, S. E. Yuter, R. A. Weller, D. Baumgardner, K. Comstock, and R. Wood: 2004, The EPIC 2001 stratocumulus study. *Bull. Am. Meteorol. Soc.*, **85**, 967–977.

Cahalan, R. F., W. Ridgway, W. J. Wiscombe, T. L. Bell, and J. B. Snider: 1994, The albedo of fractal stratocumulus clouds. *J. Atmos. Sci.*, **51**, 2434–2455.

Cahalan, R. F. and J. B. Snider: 1989, Marine stratocumulus structure. *Rem. Sens. Environ.*, **28**, 95–107.

Castleman, K. R.: 1996, *Digital image processing*. Prentice Hall.

Clark, C. and J. Boyce: 1999, The detection of ship trail clouds by artificial neural network. *Int. J. Remote Sensing*, **20**, 711–726.

Considine, G., J. A. Curry, and B. Wielicki: 1997, Modeling cloud fraction and horizontal variability in marine boundary layer clouds. *J. Geophys. Res.*, **102**, 13517–13525.

Cuijpers, J. W. M. and P. Bechtold: 1995, A simple parameterization of cloud water related variables for use in boundary layer models. *J. Atmos. Sci.*, **52**, 2846–2490.

Cusack, S., J. M. Edwards, and R. Kershaw: 1999, Estimating the subgrid variance of saturation,

and its parametrization for use in a gcm cloud scheme. *Quart. J. Roy. Meteorol. Soc.*, **12**, 3057–3076.

Davis, A., A. Marshak, H. Gerber, and W. J. Wiscombe: 1999, Horizontal structure of marine boundary layer clouds from cm to km scales. *J. Geophys. Res.*, **104**, 6123–6144.

Davis, A., A. Marshak, W. Wiscombe, and R. Cahahlan: 1996, Scale invariance of liquid water distributions in marine stratocumulus. Part 1: Spectral properties and stationarity issues. *J. Atmos. Sci.*, **53**, 1538–1558.

Fu, Q. and K.-N. Liou: 1992, On the correlated k-distribution method for radiative transfer in nonhomogenous atmospheres. *J. Atmos. Sci.*, **49**, 2139–2156.

Han, Q., W. B. Rossow, and A. A. Lacis: 1994, Near global survey of effective droplet radii in liquid water clouds using isccp data. *J. Clim.*, **7**, 465–497.

Jeffery, C. A. and P. H. Austin: 2003, Unified treatment of the thermodynamic and optical variability of unresolved low clouds. *J. Atmos. Sci.*, **60**, 1621–1631.

King, M. D., Y. Kaufman, W. P. Menzel, and D. Tanré: 1992, Remote sensing of cloud, aerosol, and water vapor properties from the moderate resolution imaging spectroradiometer (modis). *IEEE Trans. Geosci. Rem. Sens.*, **30**, 2–27.

King, M. D., S.-C. Tsay, S. E. Platnick, M. Wang, and K.-N. Liou: 1997, Cloud retrieval algorithms for modis: Optical thickness, effective particle radius, and thermodynamic phase. MODIS Algorithm Theoretical Basis Document ATBD-MOD-05, NASA.

Larson, V. E., R. Wood, P. R. Field, J.-C. Golaz, T. H. Vonder Haar, and W. R. Cotton: 2001,

Systematic biases in the microphysics and thermodynamics of numerical models that ignore subgrid-scale variability. *J. Atmos. Sci.*, **58**, 1117–1128.

Lewellen, W. S. and S. Yoh: 1993, Binormal model of ensemble patial cloudiness. *J. Atmos. Sci.*, **50**, 1228–1237.

Lovejoy, S. D.: 1982, Area-perimeter relation for rain and cloud areas. *Science*, **216**, 185–187.

Ma, X., Z. Wan, C. Moeller, W. Menzel, L. Gumley, and Y. Zhang: 2000, Retrieval of geophysical parameters from moderate resolution imaging spectroradiometer thermal infrared data: evaluation of a two-step physical algorithm. *Appl. Optics*, **39**, 3537–3550.

Marshak, A., A. Davis, W. Wiscombe, and R. Cahalan: 1997, Scale invariance in liquid water distributions in marine stratocumulus. Part II: multifractal properties and intermittency issues. *J. Atmos. Sci.*, **54**, 1423–1444.

Mellor, G. L.: 1977, The Gaussian cloud model relations. *J. Atmos. Sci.*, **34**, 356–358.

Nicholls, S. and J. Leighton: 1986, An observational study of the structure of stratiform cloud sheets: Part i. structure. *Quart. J. Roy. Meteorol. Soc.*, **112**, 431–460.

Oreopoulos, L. and R. Davies: 1998a, Plane parallel albedo biases from satellite observations. Part I: Dependence on resolution and other factors. *J. Clim.*, **11**, 919–932.

— 1998b, Plane parallel albedo biases from satellite observations. Part II: Parameterizations for bias removal. *J. Clim.*, **11**, 933–944.

Paluch, I. R. and D. H. Lenschow: 1991, Stratiform cloud formation in the marine boundary layer. *J. Atmos. Sci.*, **48**, 2141–2158.

Park, S., C. B. Leovy, and M. A. Rozendaal: 2004, A new single column marine boundary layer cloud model. *J. Atmos. Sci.*, submitted.

Peitgen, H.-O. and D. Saupe: 1988, *The science of fractal images*. Springer Verlag.

Pincus, R. and S. A. Klein: 2000, Unresolved spatial variability and microphysical process rates in large scale models. *J. Geophys. Res.*, **105**, 27059–27066.

Rand, H. A.: 1995, Mesoscale dynamics of the marine atmospheric boundary layer. *PhD thesis, University of Washington, Seattle, WA, USA*.

Rossow, W. B., C. Delo, and B. Cairns: 2002, Implications of the observed mesoscale variations of clouds for earth's radiation budget. *J. Clim.*, **15**, 557–585.

Rossow, W. B. and R. A. Schiffer: 1991, ISCCP cloud data products. *Bull. Am. Meteorol. Soc.*, **72**, 2–20.

Rotstayn, L. D.: 2000, On the "tuning" of autoconversion parameterizations in climate models. *J. Geophys. Res.*, **105**, 15,495–15,507.

Schroder, M., R. Bennartz, L. Schuller, R. Preusker, P. Albert, and J. Fischer: 2002, Generating cloudmasks in spatial high-resolution observations of clouds using texture and radiance information. *Int. J. Remote Sensing*, **23**, 4247–4261.

Smith, R. N. B.: 1990, A scheme for predicting layer clouds and their water content in a general circulation model. *Q. J. R. Meteorol. Soc.*, **116**, 435–460.

Sommeria, G. and J. W. Deardorff: 1977, Subgrid-scale condensation in models of nonprecipitating clouds. *J. Atmos. Sci.*, **34**, 344–355.

Stevens, B., G. Vali, K. Comstock, R. Wood, M. VanZanten, P. H. Austin, and D. H. Bretherton C. S.ãnd, Lenschow: 2004, Pockets of open cells (POCs) and drizzle in marine stratocumulus. *J. Atmos. Sci.*, in review.

Stull, R. B.: 1988, *An introduction to boundary layer meteorology*. Kluwer Academic Publishers.

Szczodrak, M., P. H. Austin, and P. B. Krummel: 2001, Variability of optical depth and effective radius in marine stratocumulus clouds. *J. Atmos. Sci.*, **58**, 2912–2926.

Tompkins, A. M.: 2002, A prognostic parameterization for the subgrid-scale variability of water vapor and clouds in large-scale models and its use to diagnose cloud cover. *J. Atmos. Sci.*, **59**, 1917–1942.

Van der Hoven, I.: 1957, Power spectrum of horizontal wind speed in the frequency range from 0.0007 to 900 cycles per hour. *J. Meteorol.*, **14**, 160–164.

Williams, K. D., M. A. Ringer, and C. A. Senior: 2003, Evaluating the cloud response to climate change and current climate variability. *Clim. Dyn.*, **20**, 705–721.

Wood, R.: 2004, Drizzle in stratocumulus: Part I. Vertical and horizontal structure. *J. Atmos. Sci.*, submitted.

Wood, R. and C. S. Bretherton: 2004, Boundary layer depth, entrainment and decoupling in the cloud-capped subtropical and tropical marine boundary layer. *J. Clim.*, **17**, 3576–3588.

Wood, R., P. R. Field, and W. R. Cotton: 2002, Autoconversion rate bias in boundary layer cloud parameterizations. *Atmos. Res.*, **65**, 109–128.

Wood, R. and J. P. Taylor: 2001, Liquid water path variability in unbroken marine stratocumulus. *Quart. J. Roy. Meteorol. Soc.*, **127**, 2635–2662.

Figure Captions

Figure 1: The two regions (NE and SE Pacific) in this study. Contours show fraction of 256×256 km scenes containing only warm cloud ($T_{top} > 273$ K). Grayscale shading shows ISCCP mid+high cloud amount for Sept/Oct 1984-1999.

Figure 2: Example scenes of MODIS liquid water path in boundary layer cloud showing wide variability in cloud structure. Each scene size is 256×256 km at 1 km resolution. Image times and locations are given in Table 2.

Figure 3: (a) Examples of LWP pdfs for the four test scenes shown in Fig. 2. The observed pdf is shown using filled circles. Also shown are the model pdfs for the lognormal (dotted curve) and gamma distributions with parameters estimated from the method of moments (solid curve) and from the MLE (dashed curve).

Figure 3: (b) As for Fig. 3(a) but with logarithmic axes.

Figure 4: Skewness-γ_{LWP} (a) and kurtosis-γ_{LWP} (b) frequency distribution (contours) from all SE Pacific MODIS scenes. Median values of skewness S and kurtosis K for γ_{LWP} intervals are shown (filled circles). Lines show relationships for the model pdfs.

Figure 5: Cumulative contribution to the moment of order 0.5 from LWP values smaller than

those on the abscissa for the four test scenes shown in Fig. 2. Symbols and curves are the same as those in Fig. 3. All curves are normalised with the observed moment for the full distribution. In all cases the model distribution quite accurately simulate the contributions to the moment from the different LWP values. The best agreement is found for the gamma distribution with γ_{MLE}.

Figure 6: As Fig. 5 but for moment order 3. For higher order moments the lognormal distribution is clearly an inadequate model because the contributions from high LWP values (the distribution tail) are too large. The gamma distribution using the method of moments or the MLE both perform well, as do the Gaussian-h and Gaussian-s models.

Figure 7: Cloud fraction-conditional probability contours (shaded) of γ_{LWP} for all the SE Pacific MODIS scenes. The contours represent 5th, 10th, 25th, 75th, 90th and 95th percentiles. Median CF-conditional values of γ_{LWP} are also shown (filled circles) together with the unique relationship for the Gaussian model.

Figure 8: $CF - \gamma_{LWP}$ for the most "stationary" scenes (open circles) and the most "non-stationary" scenes (filled circles). The error bar limits show the 25th and 75th percentiles for each dataset. The Gaussian model curve is denoted by the solid line.

Figure 9: Cloud fraction CF vs γ_{LWP} for SE Pacific scenes with minimum LWP thresholds of 5 g m^{-2} (solid circles) and zero (open circles). Also shown is the Gaussian model results with $LWP_{thresh} = 5$ g m^{-2} applied. Agreement between observations and models is considerably better for thresholded data. Error bars ($LWP_{thresh} = 5$ g m^{-2} MODIS data) show the 25th and 75th

percentiles. Lines in light gray are model curves for non-thresholded LWP, i.e. those in Fig. 7.

Figure 10: $\overline{LWP}$ (dotted lines) and CF (dashed lines) in the [$\overline{h}$,σ_h] plane for the Gaussian-h model 1:1 mapping. Upper and right axes show equivalent $\overline{s_i}$ and σ_s for Gaussian-s model with zero cloud top height fluctuations and Γ_{ad}=2 g kg^{-1} km^{-1}. Contours show joint pdf of values from all SE Pacific MODIS data, and contain 95%, 80%, 50%, 30%, and 10% of all scenes.

Figure 11: Joint probability distribution of τ shape parameter γ_τ and γ_{LWP}. Contours contain 98% of the scenes; filled circles are median γ_τ as a function of γ_{LWP}. Darker shaded region shows the range of values that would be obtained if there is no correlation between LWP and $r_{e,top}$, and given the observed range of $\gamma_{r_e}/\gamma_{LWP}$ (see inset). Lighter shaded region shows range for zero correlation between LWP and droplet concentration N_d, for observed range of LWP and N_d variability. Dash-dot line shows the relationship for an adiabatic cloud with homogeneous droplet concentration (i.e. $\tau = LWP^{5/6}$) and an assumed Γ distribution for LWP.

Figure 12: (a) Albedo biases as a function of CF for solar zenith angles θ_0 corresponding to MODIS scenes ($\sim 20^\circ$) expressed as the reduction ΔCF in cloud fraction CF necessary to obtain the same scene-mean albedo when homogeneity is assumed in the cloudy portion of the scene. Shaded regions show the 5th, 10th, 25th, 75th, 90th and 95th percentiles for the spherical albedo. Solid circles denote median values. Also shown are results for θ_0=0,45 and 60°; (b) Median ΔCF as a function of θ_0 for three CF ranges.

Figure 13: Power spectra calculated using 2D-FFT for the four example scenes shown in

Fig. 2. The unsmoothed spectra are shown using the solid line. Spectra are normalised so that $\int_0^\infty P_{LWP} dk = \sigma^2_{LWP,all}$ where $\sigma_{LWP,all}$ is the standard deviation of LWP (including cloud free regions where $LWP = 0$). Averaged spectra are shown using filled circles and approximate 95% confidence limits are given by the light dotted line. The filled triangle on the wavenumber axis shows the "mean" wavenumber used to determine the power law fit to the large k end of the observed spectra (thick dotted line). The two characteristic lengthscales are defined as λ_1, the wavelength of the highest wavenumber peak in the averaged power spectrum. λ_2, the minimum wavenumber at which the 95% confidence limit of the spectrum exceeds the fitted power law. These scales correspond approximately to cellular diameters and cloud-sizes respectively.

Figure 14: Averaged power spectra four different ranges of the characteristic cell lengthscale λ_1. Vertical gray bars indicate extent of λ_1 ranges. Data are taken from the NE Pacific region only; spectra are almost identical for the SE Pacific data.

Figure 15: Probability distribution of $\alpha = \overline{\sigma_{i,j}}/\sigma_{\overline{x_{i,j}}}$ for all MODIS NE and SE Pacific 2×2-scene regions containing $> 10\%$ cloud. Solid line shows distribution resulting from simulations with LWP spatial maps generated with an inverse FFT fractal cascade for which the ensemble scaling expondent is specified to be $\beta = -5/3$. Error bars show the 95% confidence limits for the observed distributions. Vertical lines show the median values of α for the observations. Inset shows the median value of α as a function of β showing that the MODIS observations are well modeled (horizontal lines show the median values from observations) by a fractal cascade with a scaling exponent close to -5/3.

Figure 16: Probability distribution functions of cloud fraction CF for the four scene-type categories.

Figure 17: Fraction of all scenes classified into each of the four categories as a function of MBL depth z_i.

Table 1: Details of the regions examined in this study.

Region	Longitude range	Latitude range	Period [mm/dd/yy]	Scenes analyzed [number]
NE Pacific	110-150W	10-50N	08/20/00-10/31/00	7803
SE Pacific	70-120W	30S-10N	09/01/00-10/31/00	12992

Table 2: Characteristics of the four test images shown in Fig. 2. Parameters listed are cloud fraction CF; characteristic scale of the cells λ_1 and of the cloud structures λ_2; mean liquid water path $\overline{LWP}$; the ratio of square of the mean mean to the variance of LWP for cloudy pixels only, calculated directly (γ) and using the MLE method (γ_{MLE}); liquid water path skewness S_{LWP}; Type of cloud formation (open cells O, closed cells C, or homogeneous H); boundary layer depth z_i.

Image	Date	Location [lat,long]	CF	λ_1 [km]	λ_2 [km]	$\overline{LWP}$ [g m^{-2}]	γ	γ_{MLE}	S_{LWP}	Type	z_i [m]
(a)	17 Oct 00	36N,125W	0.99	5.4	N/A[1]	58	5.02	3.72	0.51	H	610
(b)	18 Aug 00	30N,131W	0.88	10.9	10.3	58	3.13	2.97	1.45	C	760
(c)	18 Aug 00	26N,135W	0.86	38.5	48.2	72	1.35	1.37	1.38	C	1100
(d)	13 Oct 00	11S,97W	0.32	35.7	10.1	29	1.24	1.40	1.72	O	1020

Notes: [1] Characteristic scale undetermined.

Table 3: Forms for the liquid water path LWP pdf examined in this study

Name	Description/Refs
Gamma pdf (Γ);	see Barker (1996a)
Lognormal pdf (LN);	see Oreopoulos and Davies (1998a)
Gaussian-h pdf	The LWP pdf that results from the assumption that in the cloud layer thermodynamic profiles are locally moist adiabatic, with a cloud thickness h that is a Gaussian random variable.
Gaussian-s pdf	The LWP pdf resulting from the assumption of a uniform cloud top height and that at each level below this the saturation excess is distributed using a Gaussian form. The saturation excess pdf width is constant with height and the mean increases linearly with height (adiabatic model). Columns are assumed to be vertically coherent, i.e. the local saturation excess increases linearly with height in each column.

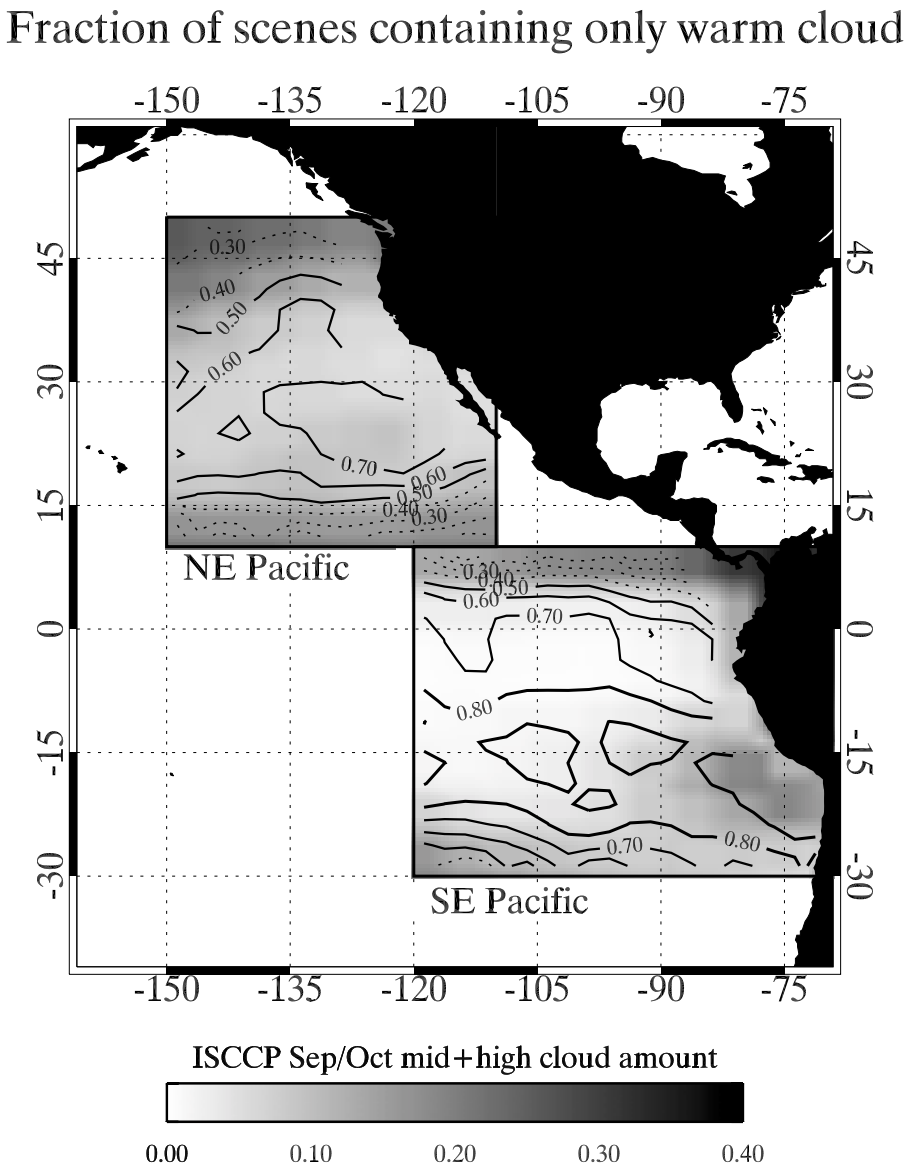
Fraction of scenes containing only warm cloud
-150
-135
-120
-105
-90
-75
45
30
15
0
-15
-30
0.30
0.40
0.50
0.60
0.70
0.80
NE Pacific
SE Pacific
ISCCP Sep/Oct mid+high cloud amount
0.00
0.10
0.20
0.30
0.40

Figure 1:

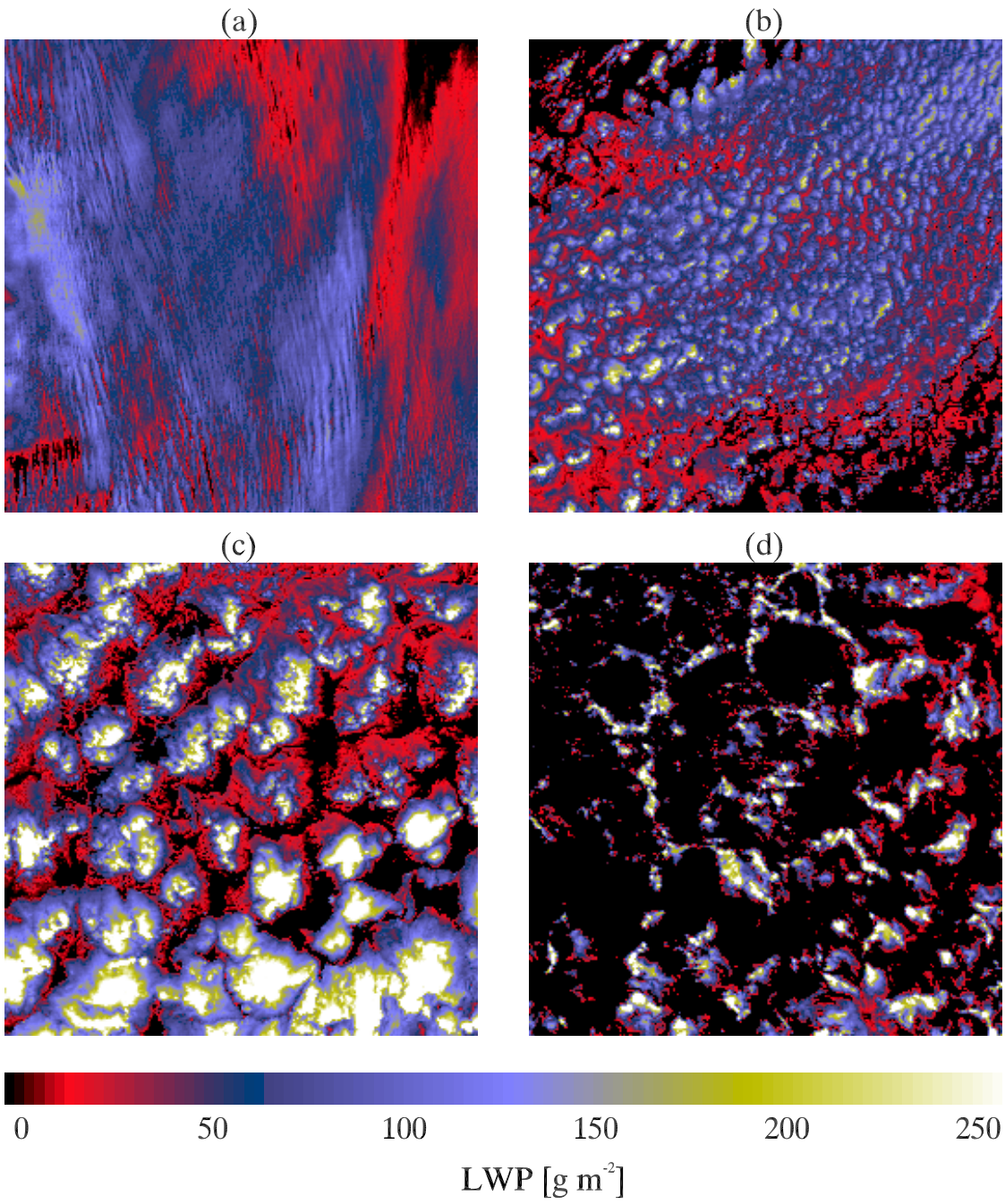

Figure 2:

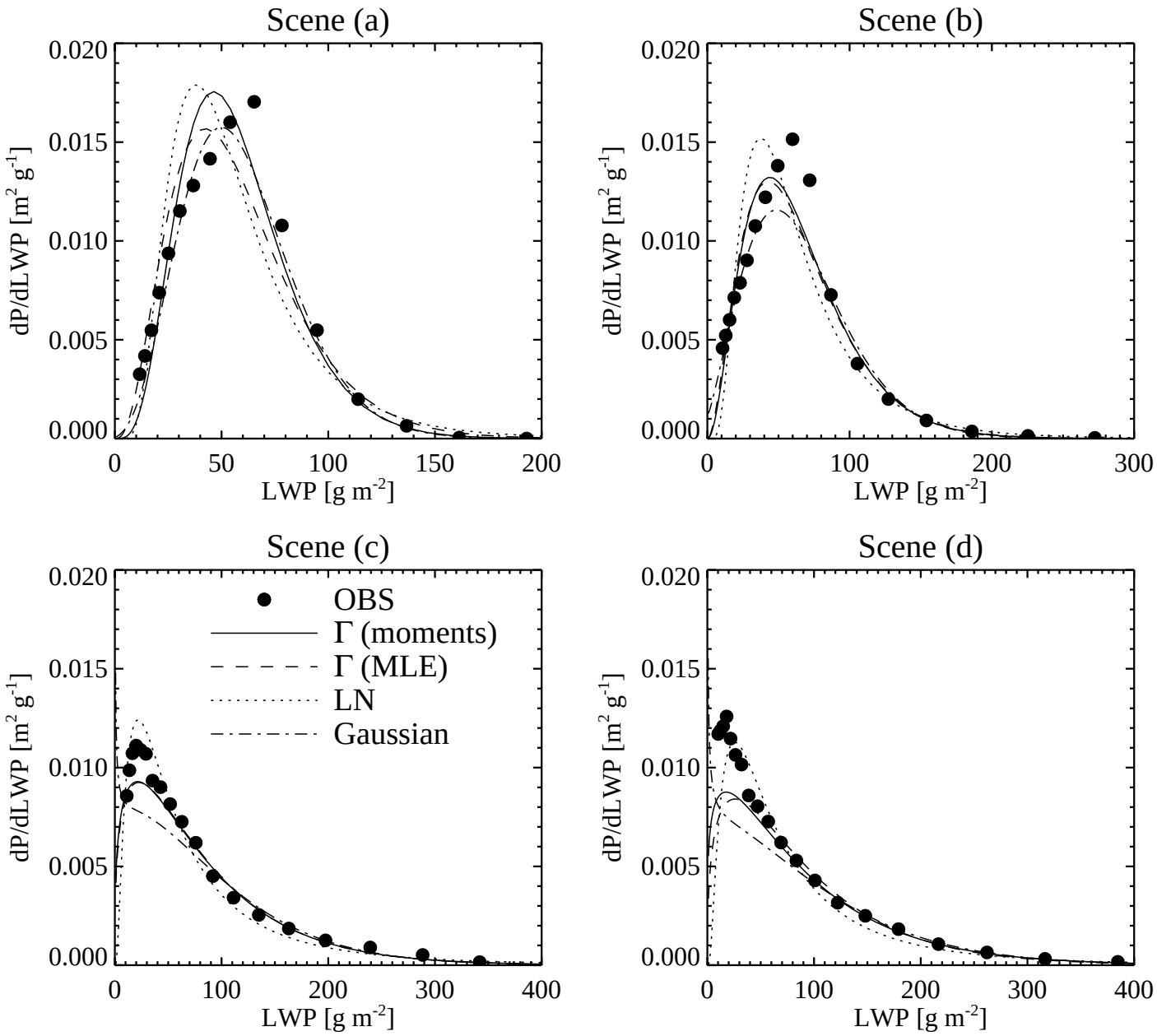
Scene (a)
Scene (b)
Scene (c)
Scene (d)
OBS
Γ (moments)
Γ (MLE)
LN
Gaussian
dP/dLWP [m^2 g^{-1}]
LWP [g m^{-2}]
0.000
0.005
0.010
0.015
0.020
0
50
100
150
200
300
400

Figure 3:

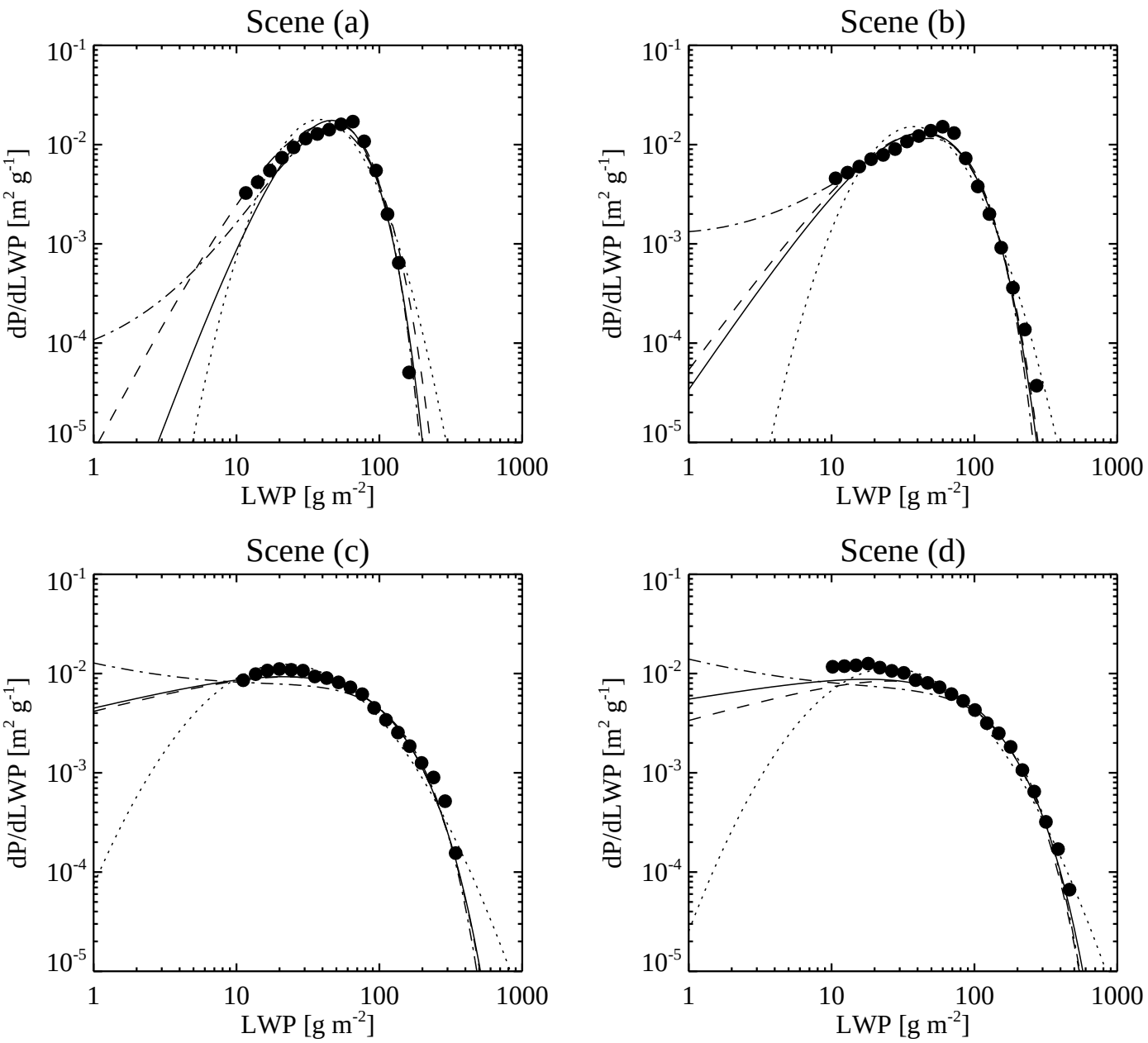
Scene (a)
Scene (b)
Scene (c)
Scene (d)
dP/dLWP [m^2 g^{-1}]
LWP [g m^{-2}]
10^{-1}
10^{-2}
10^{-3}
10^{-4}
10^{-5}
1
10
100
1000

Figure 3:

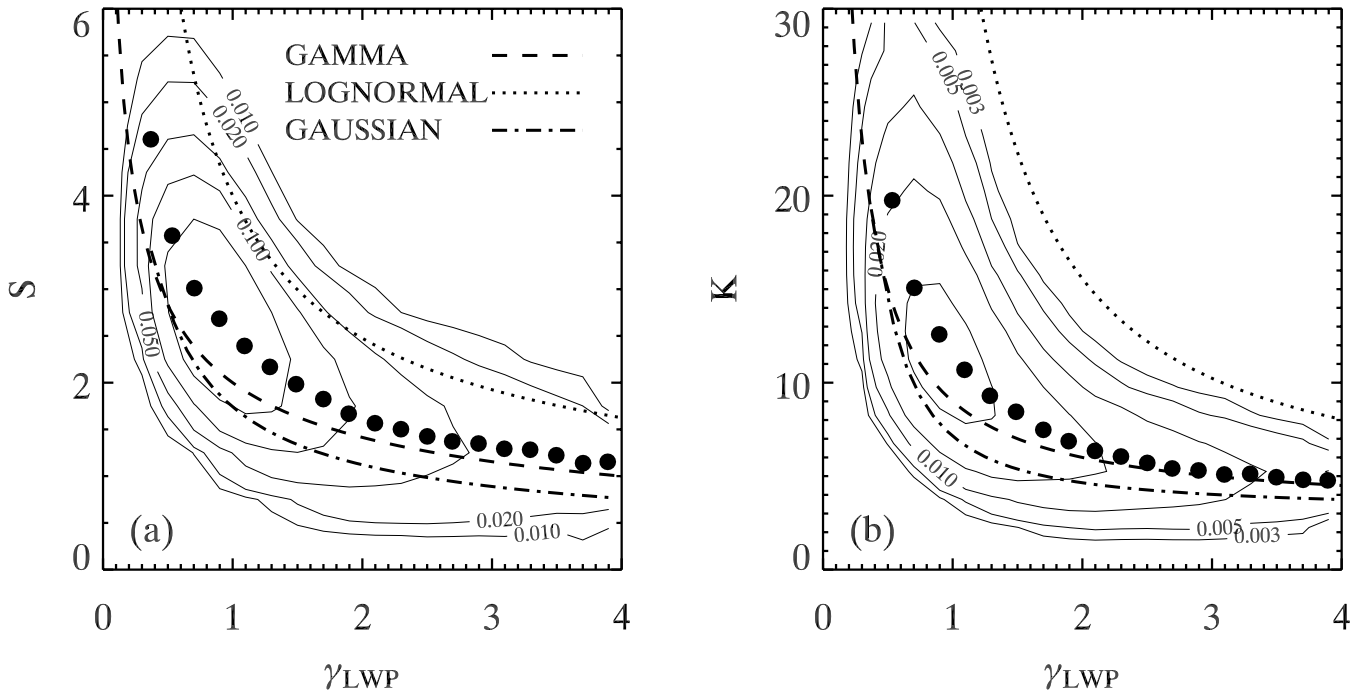
GAMMA
LOGNORMAL
GAUSSIAN
(a)
(b)
S
K
γ_{LWP}
γ_{LWP}
0.010
0.020
0.100
0.050
0.020
0.010
0.005
0.003
0.020
0.010
0.005
0.003

Figure 4:

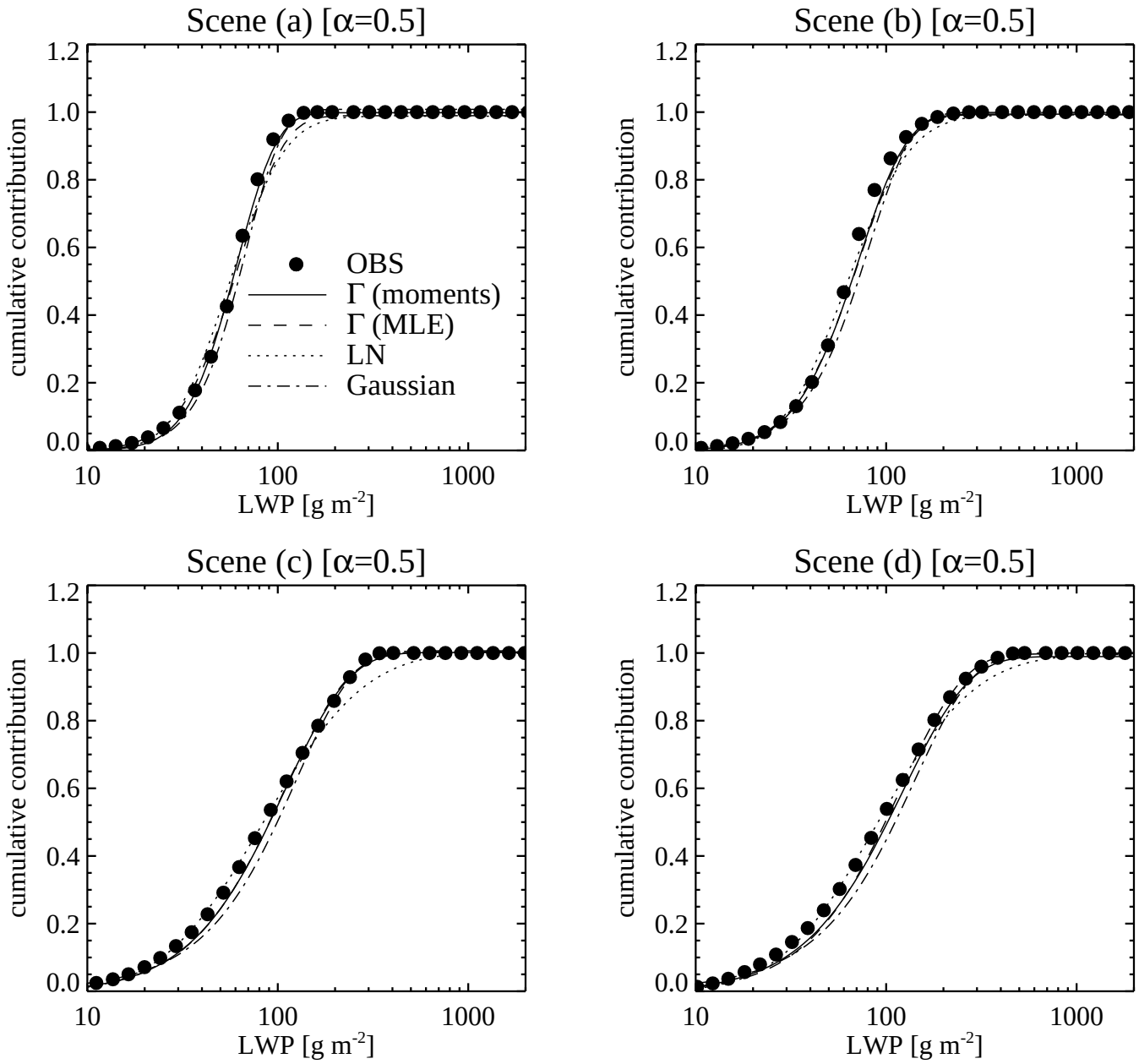
Scene (a) [α=0.5]
Scene (b) [α=0.5]
Scene (c) [α=0.5]
Scene (d) [α=0.5]
cumulative contribution
LWP [g m-2]
OBS
Γ (moments)
Γ (MLE)
LN
Gaussian
0.0
0.2
0.4
0.6
0.8
1.0
1.2
10
100
1000

Figure 5:

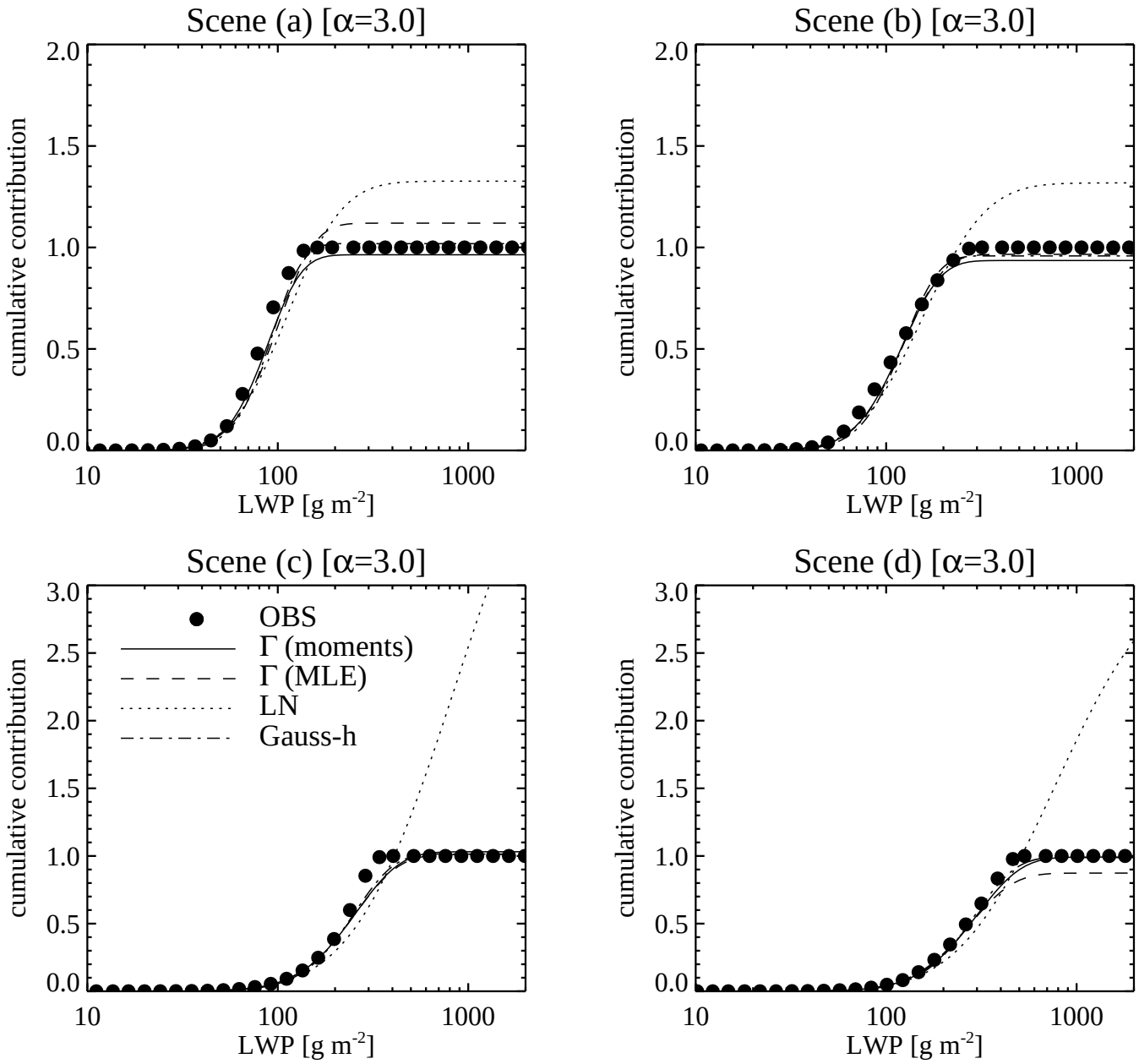
Scene (a) [α=3.0]
Scene (b) [α=3.0]
Scene (c) [α=3.0]
Scene (d) [α=3.0]
cumulative contribution
LWP [g m-2]
OBS
Γ (moments)
Γ (MLE)
LN
Gauss-h

Figure 6:

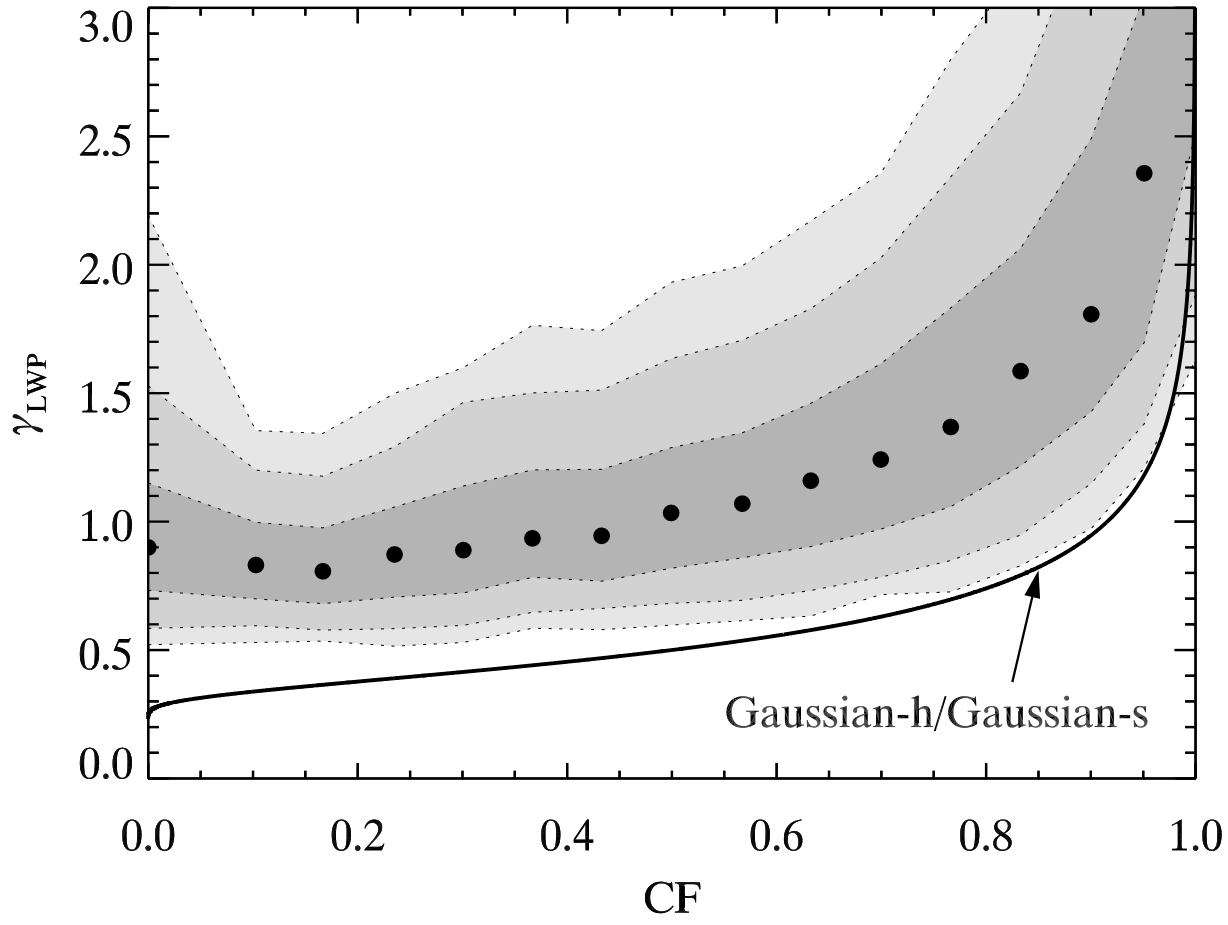
3.0
2.5
2.0
1.5
1.0
0.5
0.0
γ_{LWP}
0.0
0.2
0.4
0.6
0.8
1.0
CF
Gaussian-h/Gaussian-s

Figure 7:

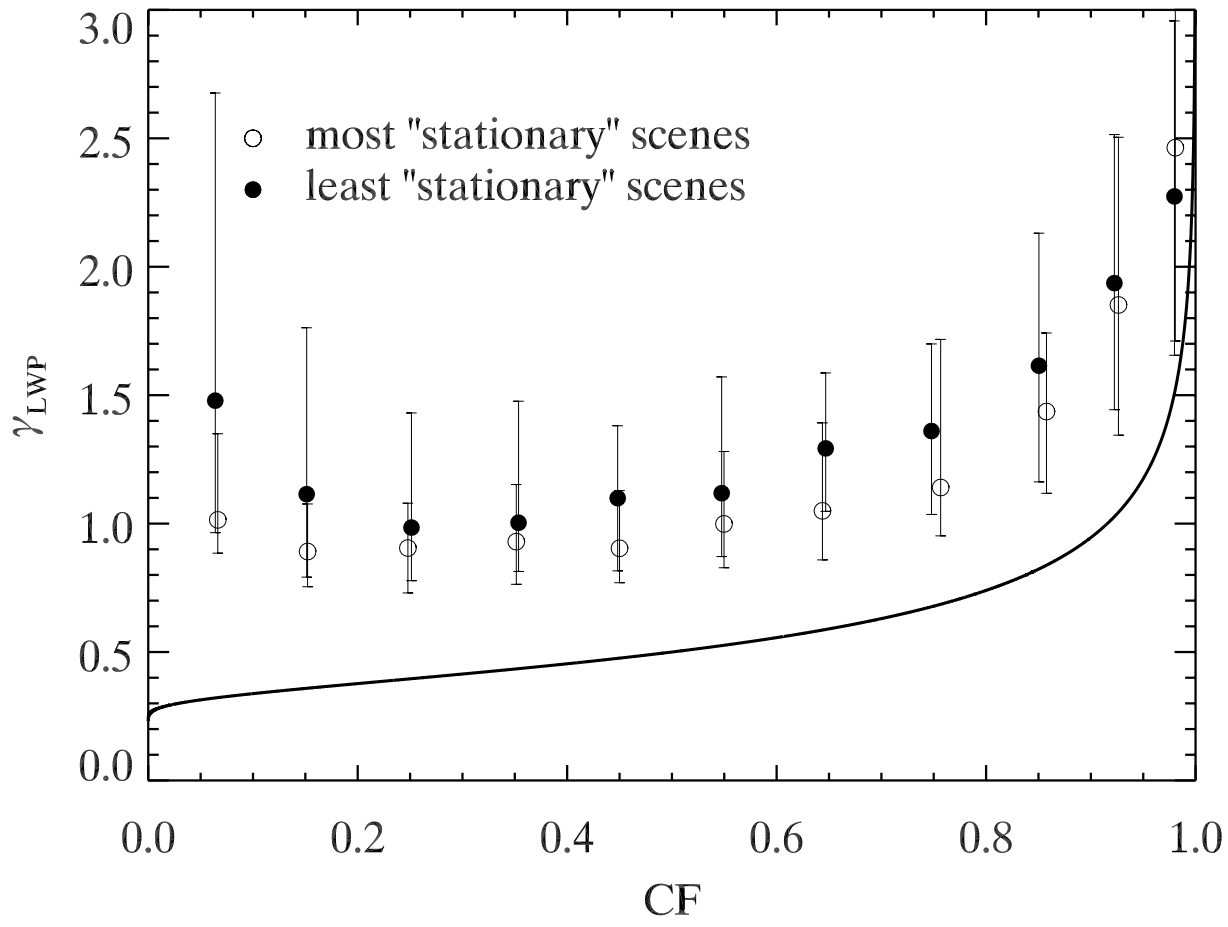
3.0
2.5
2.0
1.5
1.0
0.5
0.0
γ_{LWP}
most "stationary" scenes
least "stationary" scenes
0.0
0.2
0.4
0.6
0.8
1.0
CF

Figure 8:

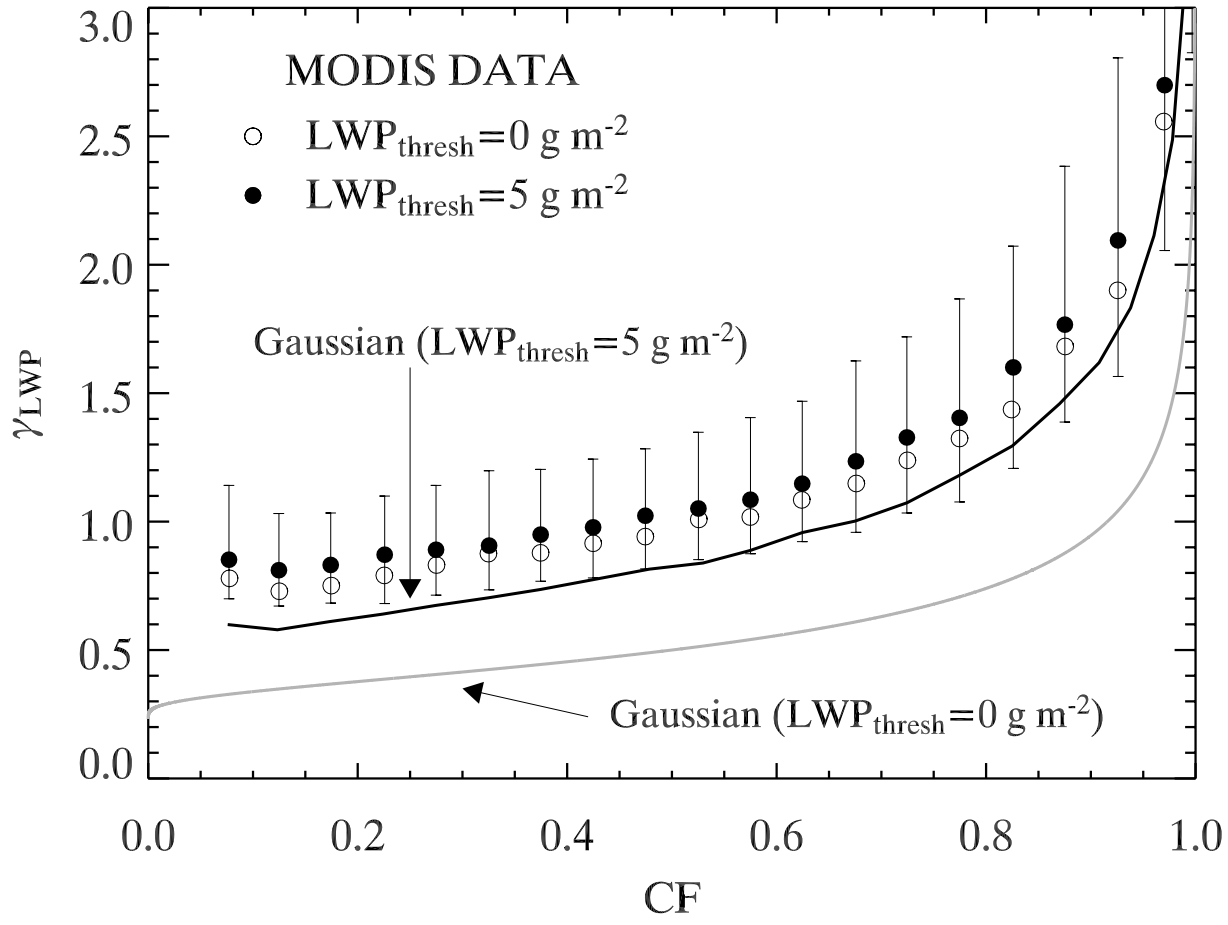
MODIS DATA
LWP$_{thresh}$=0 g m^{-2}
LWP$_{thresh}$=5 g m^{-2}
Gaussian (LWP$_{thresh}$=5 g m^{-2})
Gaussian (LWP$_{thresh}$=0 g m^{-2})
γ_{LWP}
CF
3.0
2.5
2.0
1.5
1.0
0.5
0.0
0.0
0.2
0.4
0.6
0.8
1.0

Figure 9:

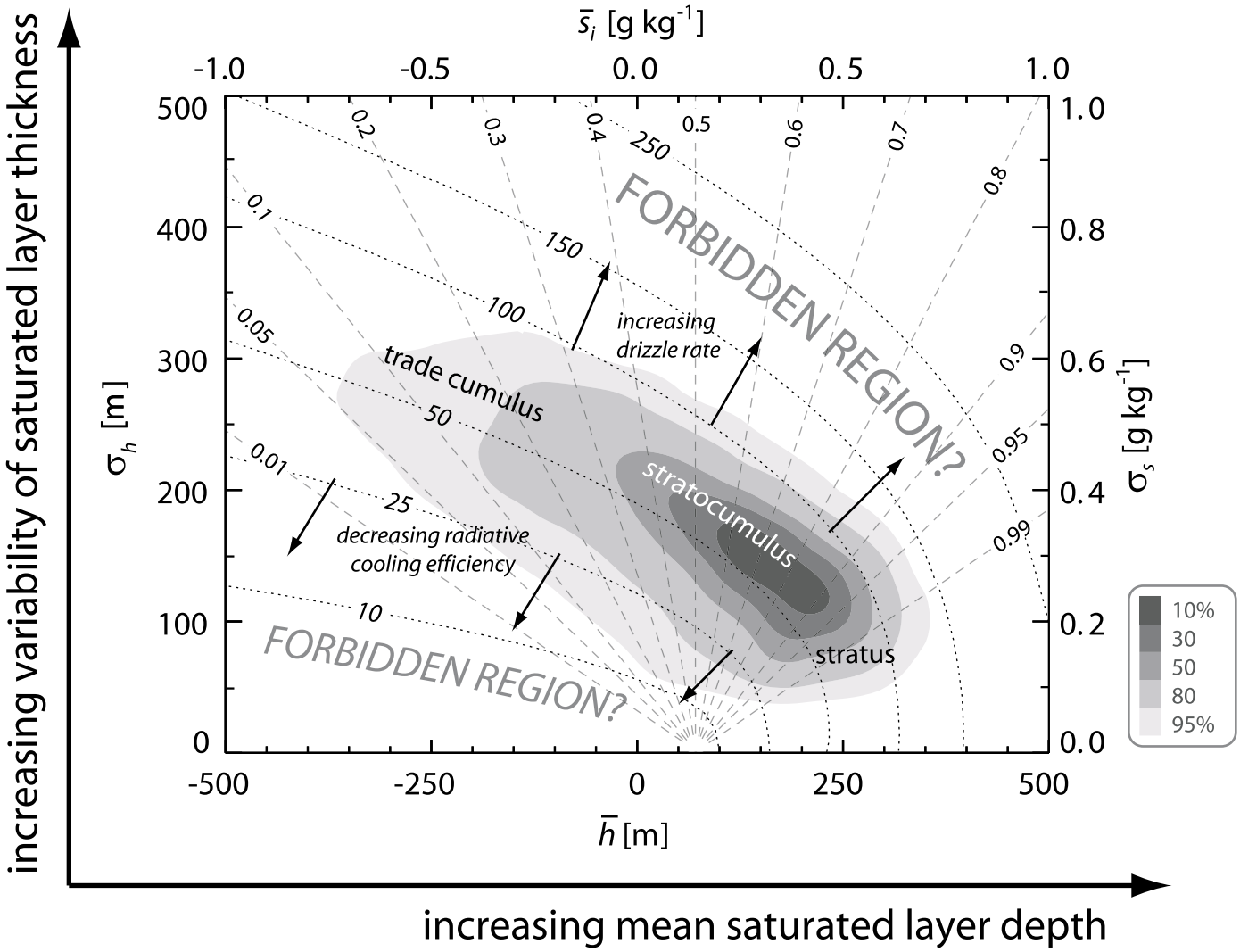
increasing variability of saturated layer thickness
increasing mean saturated layer depth
$\bar{s}_i$ [g kg^{-1}]
$\bar{h}$ [m]
σ_h [m]
σ_s [g kg^{-1}]
-1.0
-0.5
0.0
0.5
1.0
500
400
300
200
100
0
-500
-250
0
250
500
0.8
0.6
0.4
0.2
0.0
0.2
0.3
0.4
0.5
0.6
0.7
0.8
0.9
0.95
0.99
0.1
0.05
0.01
250
150
100
50
25
10
FORBIDDEN REGION?
increasing
drizzle rate
trade cumulus
stratocumulus
stratus
decreasing radiative
cooling efficiency
FORBIDDEN REGION?
10%
30
50
80
95%

Figure 10:

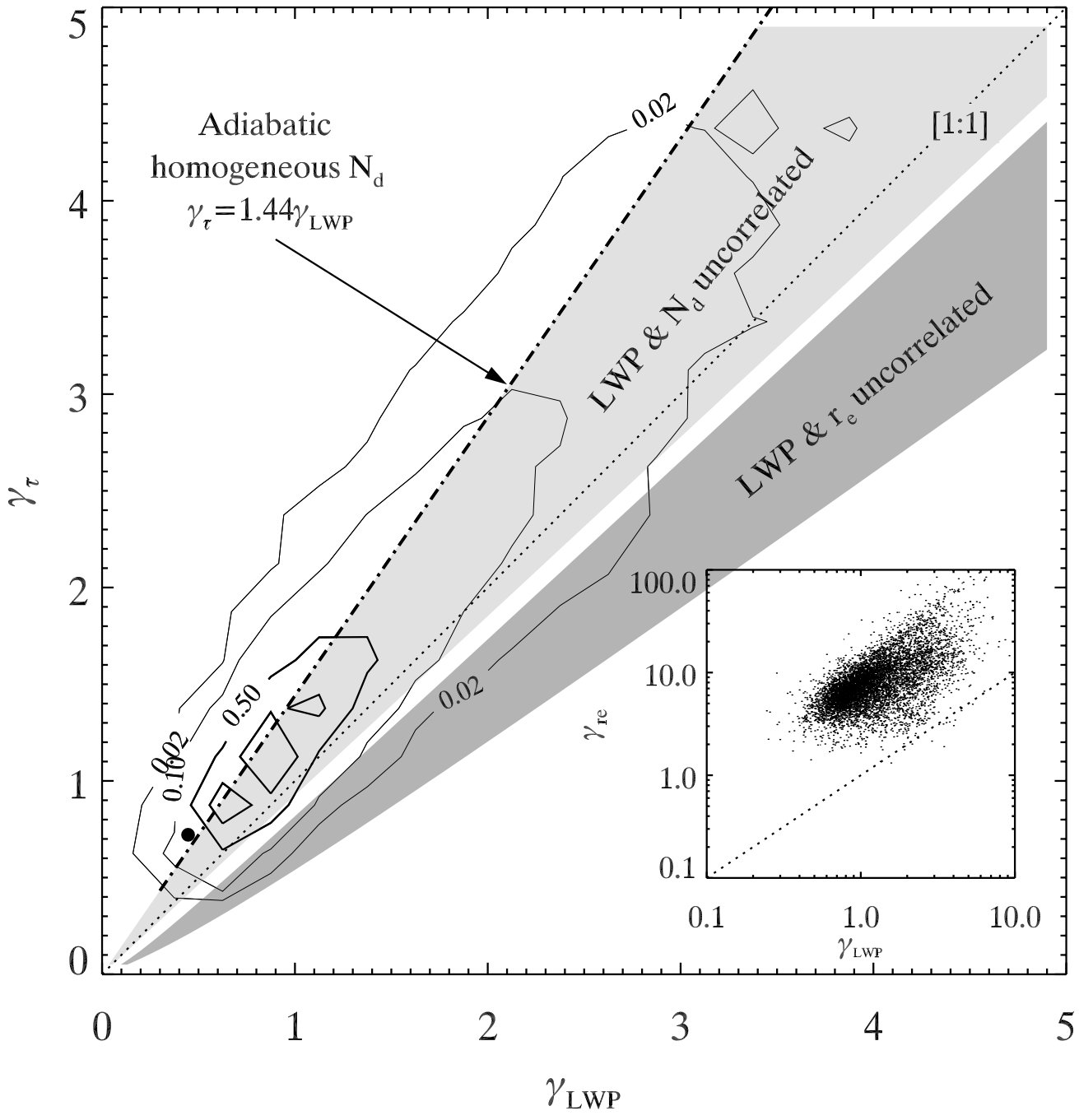
Adiabatic
homogeneous N_d
$\gamma_\tau = 1.44\gamma_{LWP}$
[1:1]
LWP & N_d uncorrelated
LWP & r_e uncorrelated
0.02
0.50
0.10
100.0
10.0
1.0
0.1
γ_{re}
γ_{LWP}
γ_τ
0
1
2
3
4
5

Figure 11:

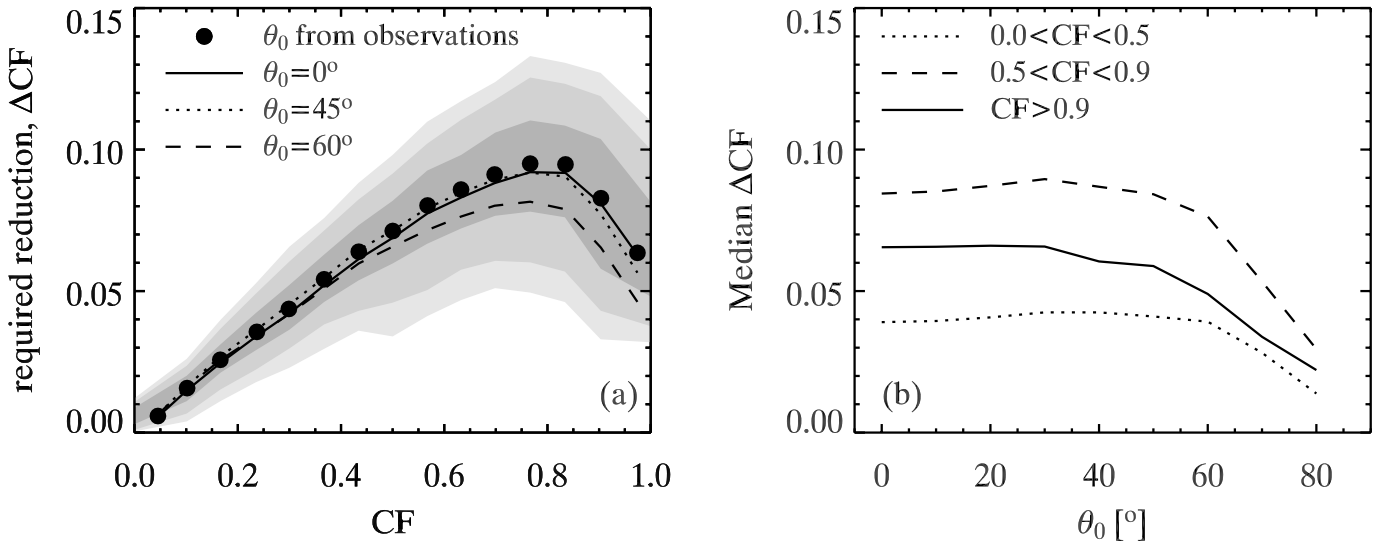
0.15
0.10
0.05
0.00
required reduction, ΔCF
θ0 from observations
θ0=0°
θ0=45°
θ0=60°
(a)
0.0
0.2
0.4
0.6
0.8
1.0
CF
Median ΔCF
0.0<CF<0.5
0.5<CF<0.9
CF>0.9
(b)
0
20
40
60
80
θ0 [°]

Figure 12:

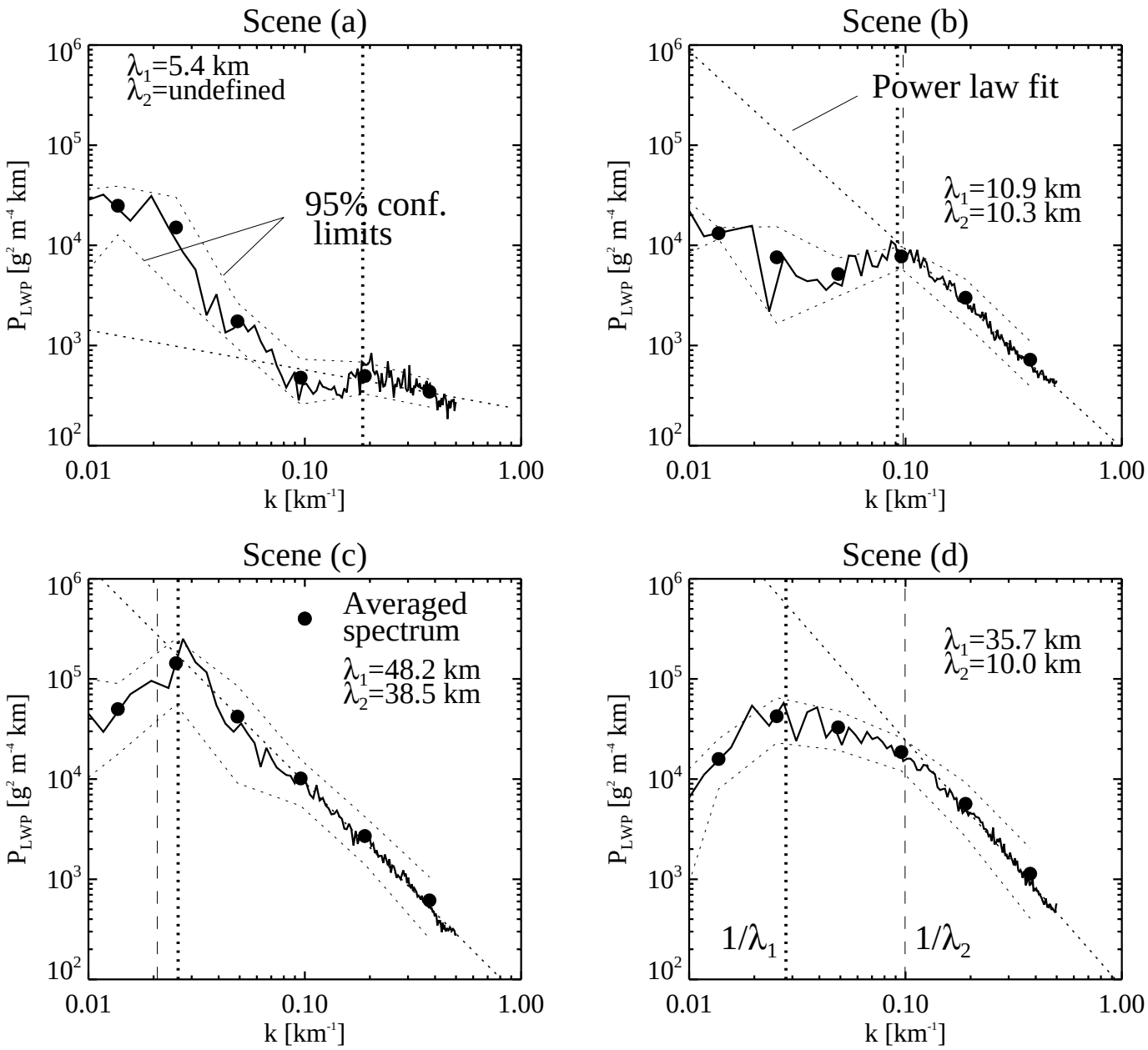
Scene (a)
λ1=5.4 km
λ2=undefined
95% conf. limits
Scene (b)
Power law fit
λ1=10.9 km
λ2=10.3 km
Scene (c)
Averaged spectrum
λ1=48.2 km
λ2=38.5 km
Scene (d)
λ1=35.7 km
λ2=10.0 km
1/λ1
1/λ2
P_LWP [g² m⁻⁴ km]
k [km⁻¹]
0.01
0.10
1.00
10²
10³
10⁴
10⁵
10⁶

Figure 13:

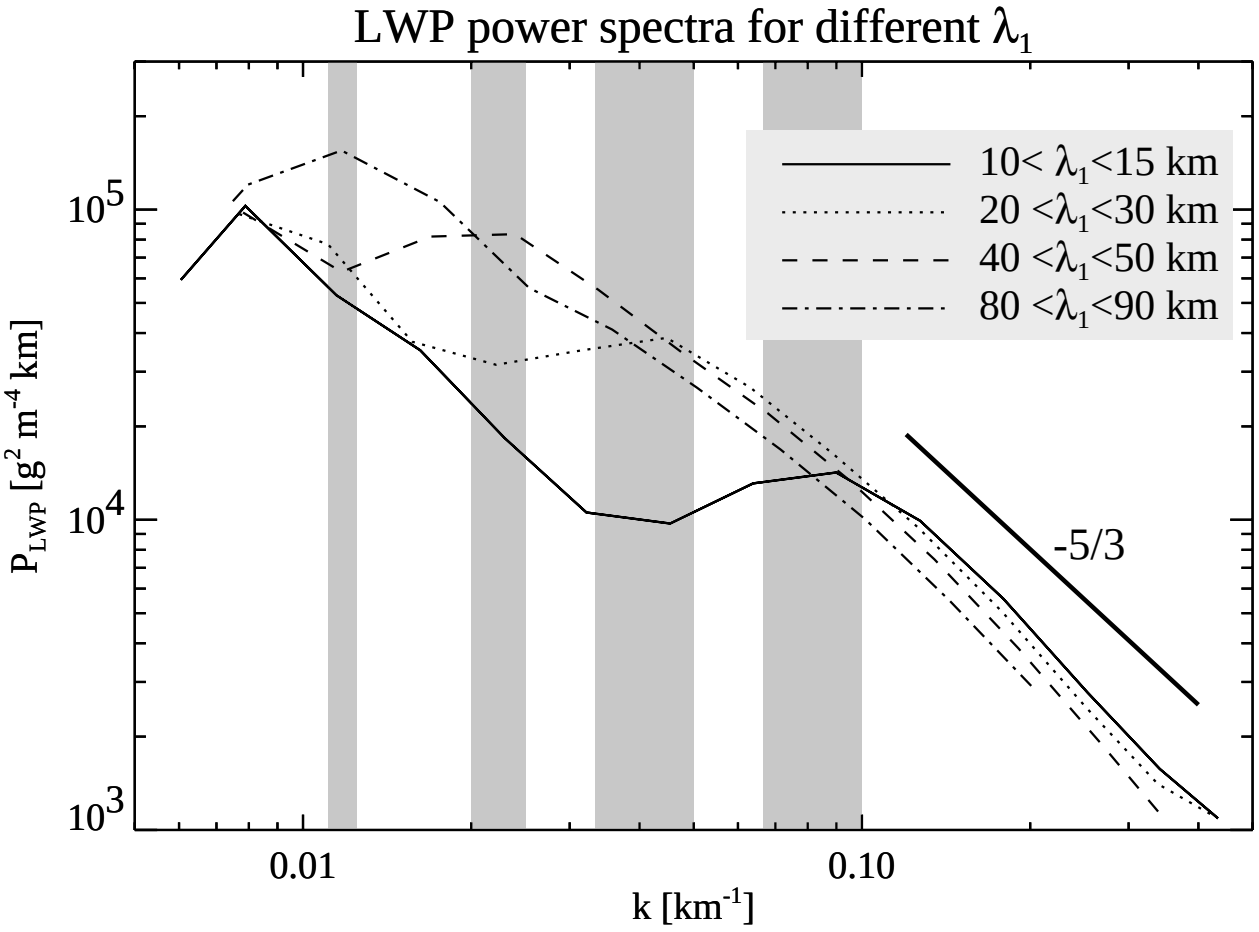
LWP power spectra for different λ1
10< λ1<15 km
20 <λ1<30 km
40 <λ1<50 km
80 <λ1<90 km
-5/3
10^5
10^4
10^3
P_LWP [g^2 m^-4 km]
0.01
0.10
k [km^-1]

(a)

Figure 14:

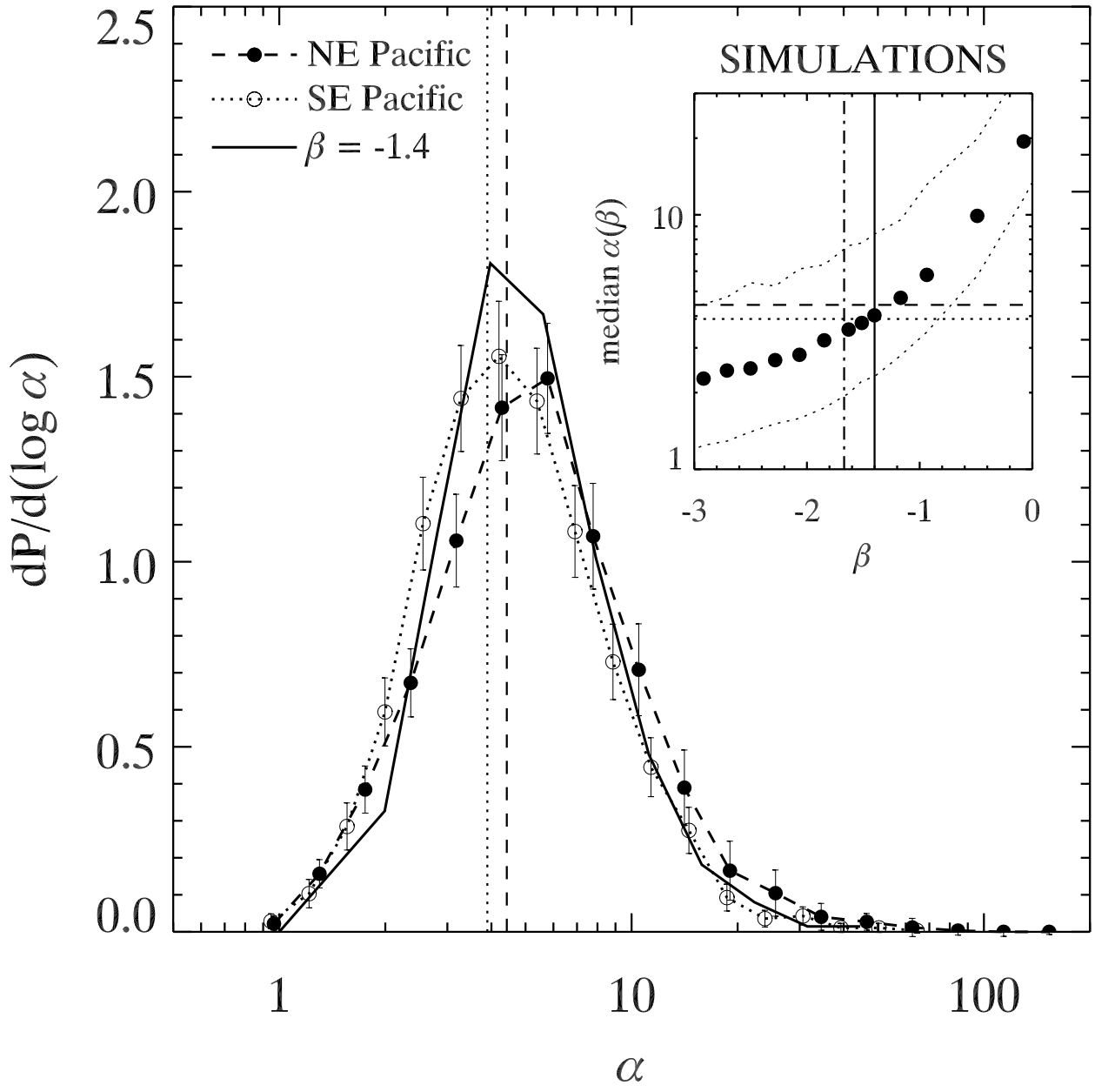
NE Pacific
SE Pacific
β = -1.4
SIMULATIONS
median α(β)
β
dP/d(log α)
α
2.5
2.0
1.5
1.0
0.5
0.0
1
10
100
-3
-2
-1
0

Figure 15:

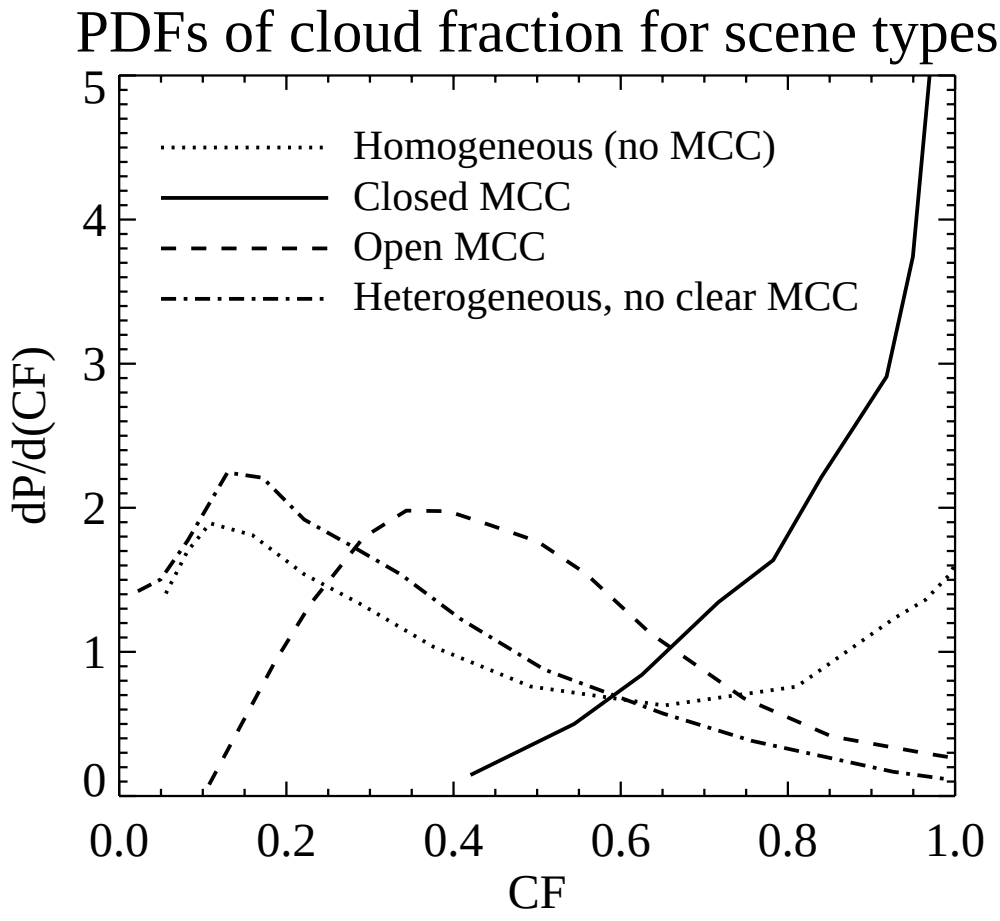
PDFs of cloud fraction for scene types
Homogeneous (no MCC)
Closed MCC
Open MCC
Heterogeneous, no clear MCC
dP/d(CF)
CF
0
1
2
3
4
5
0.0
0.2
0.4
0.6
0.8
1.0

Figure 16:

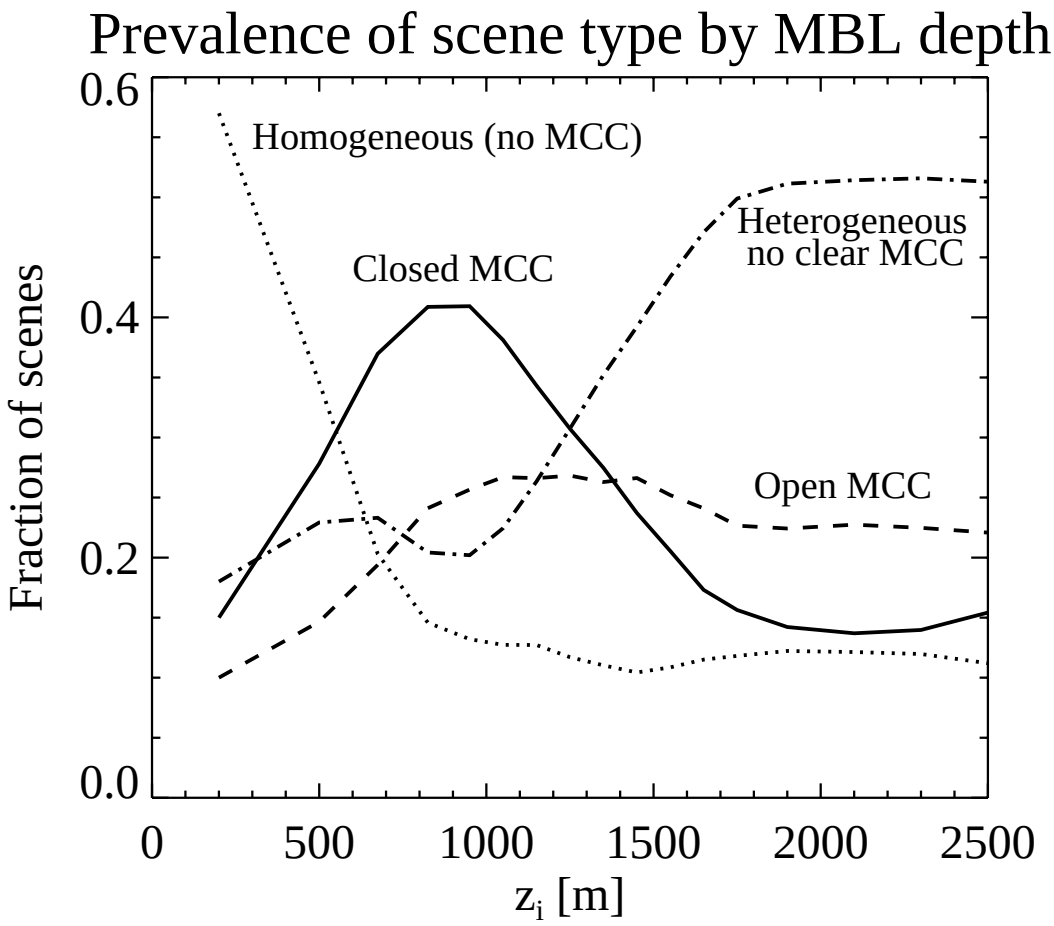
Prevalence of scene type by MBL depth
Fraction of scenes
0.6
0.4
0.2
0.0
Homogeneous (no MCC)
Closed MCC
Heterogeneous
no clear MCC
Open MCC
0
500
1000
1500
2000
2500
z_i [m]

Figure 17: